ABSTRACT

Title of dissertation: THE IMPACT OF DOUBLE LAYERS
                                ON ELECTRON TRANSPORT
                                IN THE SOLAR CORONA

                                Tak Chu Li, Doctor of Philosophy, 2013

Dissertation directed by: Professor James F. Drake
                                Department of Physics

The problem of flare-heated electron transport from the corona to the chromosphere is crucial to understanding energy release in solar flares. Observations of coronal X-ray emissions suggested two opposite scenarios: free propagation and confinement of energetic electrons. Confinement is implied in the unexplained prolonged lifetime of the electrons compared to their transit time across the source region. Theoretical modeling of electron transport in solar flares has invoked anomalous resistivity resulting in anomalous conduction. However, there has been no clear evidence for anomalous conduction in numerical simulations. We explore the mechanisms of energetic electron transport in the solar corona by particle-in-cell (PIC) simulations. We demonstrate that hot electron transport is significantly inhibited by the formation of nonlinear, highly localized electrostatic potential drops, in the form of double layers (DLs). The electrons are either reflected by the potential and therefore confined in the source or decelerated and can therefore escape. An increasing number of DLs are generated in larger-scale simulations, pointing to a more

likely picture for future space missions probing the corona. Hot electrons stream along magnetic fields through regions of cold plasma. A stream of cold return current electrons develops to maintain a system with zero net current. The DLs are generated through an ion-electron streaming instability due to the drift of the return current electrons interacting with the ions. The effectiveness of transport suppression by a DL is linked to the strength of the DL as defined by its potential drop. We demonstrate that the strength is limited by the formation of parallel shocks. Using PIC simulations and analytic modeling, we show that the maximum strength scales linearly with the hot electron temperature. At the maximum strength, a DL is capable of confining a substantial fraction of electrons in the source.

This study has important implications for electron transport during solar flares. It shows transport suppression begins when the energetic electrons start to propagate away from a coronal acceleration site. It also reveals confinement of electrons with kinetic energies less than the total potential of the DLs for the DLs' lifetime, which is much longer than the electron transit time through the source region. Our results are consistent with observations of both free propagation and confinement of X-ray producing electrons in the corona, corresponding to the escaping and reflected electrons, respectively.

THE IMPACT OF DOUBLE LAYERS ON ELECTRON TRANSPORT IN THE SOLAR CORONA

by

Tak Chu Li

Dissertation submitted to the Faculty of the Graduate School of the
University of Maryland, College Park in partial fulfillment
of the requirements for the degree of
Doctor of Philosophy
2013

Advisory Committee:
Professor James F. Drake, Chair/Advisor
Dr. Michael M. Swisdak, Co-Advisor
Professor Adil B. Hassam
Professor William D. Dorland
Professor Christopher S. Reynolds

Dedication

Dedicated to my soul sister for her endless support and encouragement while I was writing up this thesis, and always. :-)

Acknowledgments

I am truly grateful to my advisor, Jim Drake. He is being immensely supportive and selfless to my professioanal growth. From him, I see what a good researcher is. I am also very grateful and indebted to my co-advisor, Marc Swisdak. He is always there to help and teaches me so much about problem solving. I feel extremely fortunate to work with them. I would like to thank Drs. Bill Dorland, Adil Hassam and Chris Reynolds for graciously serving on my thesis committee; and Dr Thomas Antonsen for being an unofficial member. Many thanks go to my past and present collegues, Yi-Hsin Liu, Ray Fermo, Kevin Schoeffler, Haihong Che, Joel Dahlin, Lora McMurtrie and Qile Zhang, for very pleasant experience shared together. I would like to thank the diverse and friendly plasma, solar and space physics communities I interacted with at SHINE, AGU and DPP. They inspire me.

The staff at IREAP, Mohini, Nancy, Ed Condon; and at Phyaics, Jane and Linda, have been extremely helpful. The fellow students at Physics and IREAP that I have the opportunity to interact with are very nice to me. I appreciate all the enjoyable time with my previous and current officemates and their understanding. I especially would like to thank Luke for so many good times and sharing tea together; and George for his kindness and friendship. It is so much fun sharing life as a graduate student and discussing science with them.

My love goes out to my best friends and family. They make me the person I am today. I am thankful for the opportunity my dad gave me and kind wishes from my little brother. I would especially love to express my sincere gratitude to

Veronika, Joyce and Anna. They inspire me to be a better self both personally and professionally. Their support means more than I could ever put in words. Thank you from my heart for everything you do.

Table of Contents

List of Figures

viii

List of Abbreviations

DL	Double layer
HXR	hard X-ray
IA	ion-acoustic
PIC	particle-in-cell (simulation)
RC	return current
RHESSI	Reuven Ramaty High Energy Solar Spectroscopic Imager
SXR	soft X-ray
TOF	time-of-flight
TRACE	Transition Region And Coronal Explorer
THEMIS	Time History of Events and Macroscale Interactions during Substorms

T_{h0}	initial (parallel) hot electron temperature
β	plasma beta (ratio of plasma pressure to magnetic pressure)
B	magnetic field
c_A	Alfvén speed
c_{s0}	sound speed based on T_{h0}
d_e	electron inertial length
e	elementary charge
E_x	parallel electric field
erfc	complementary error function
λ_{De}	Debye length
ϕ	electric potential
ϕ_{DL}	potential drop of DL(s)
m_e	electron mass
μ	magnetic moment
n_{esp}	escaping electron density
ω_{pe}	electron plasma frequency

Chapter 1

Solar Flares and Electron Transport

1.1 Flare loops in the solar corona

The physical system under consideration is a typical flaring loop commonly observed during solar flares above the surface of the sun. Figure 1.1 shows an example of flaring loops in ultraviolet emission with the TRACE spacecraft. The emissive hot plasma traces out the magnetic field of the loops. The bright spots where the loops anchors the surface of the sun are their footpoints. The loops are also visible in X-rays. In X-rays, the loop body usually emits from thermal sources while the footpoints are from non-thermal sources. These radiation sources are energized particles from the ambient solar atmosphere produced by various mechanisms such as shocks, turbulence and magnetic reconnection (Miller et al., 1997). The energy is ultimately believed to come from the magnetic field energy released via magnetic reconnection that occurs in the high corona. Figure 1.2 shows the standard reconnection picture. Magnetic field lines annihilate at a localized reconnection site. The resulting reconnected field lines are elongated and have high magnetic tension. By slinging outwards to become round, the field lines reduce their tension and thus release their associated field energy. The field energy is converted into particle flow energy and kinetic energy by heating and accelerating particles in the outflow region.

From the reconnection outflow, energized particles flowing downwards interact
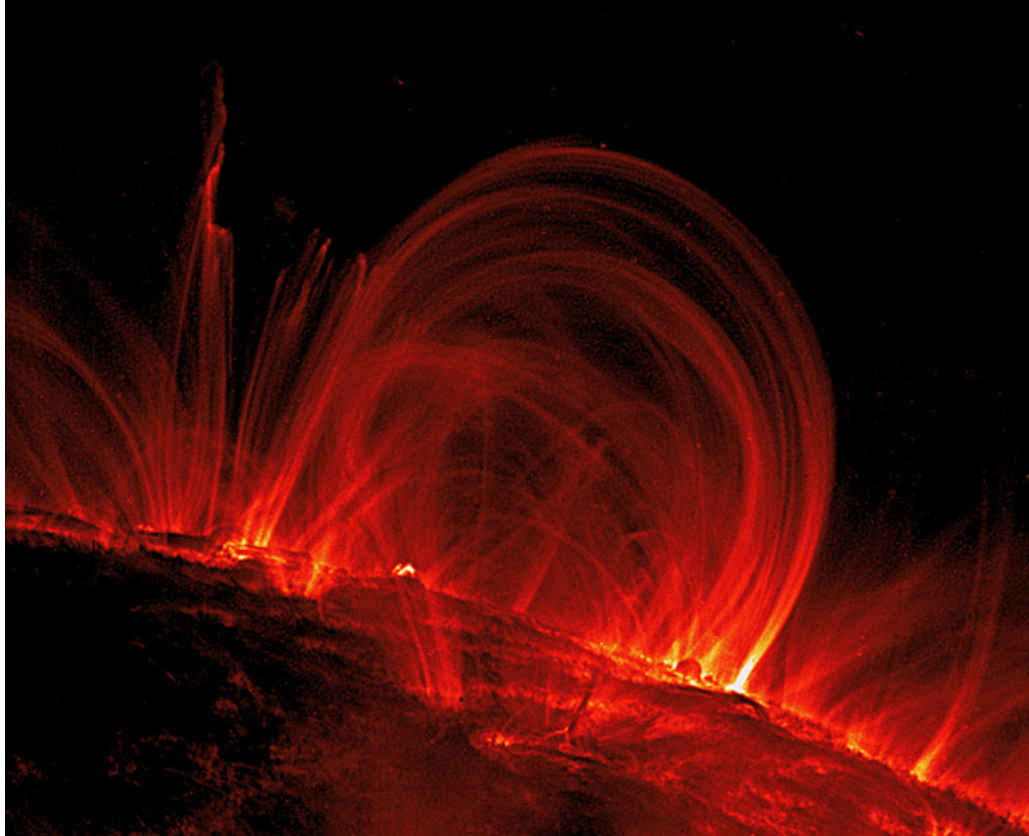
Figure 1.1: A typical flaring loop on the solar limb as seen in ultraviolet emission with the Transition Region And Coronal Explorer (TRACE) spacecraft. The magnetic field of the corona is outlined by the hot (around one million degrees Kelvin) loops (credit: NASA).
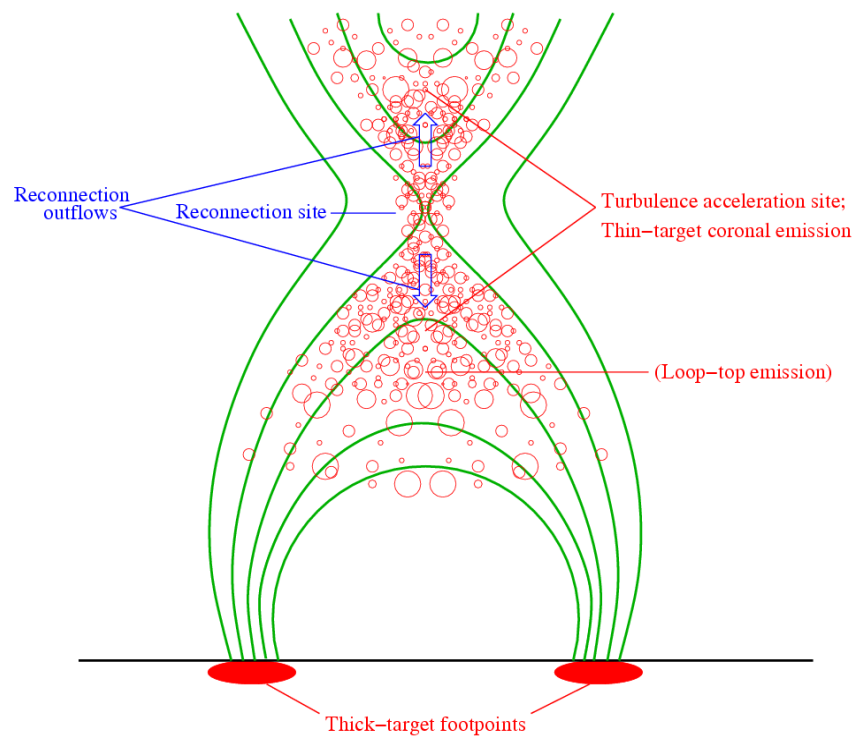
Figure 1.2: Schematic of the standard picture of magnetic reconnection that takes place in the corona. Green curves are magnetic field lines. Particles are energized in the outflow region denoted by red bubbles. Adapted with permission from Ref (Liu et al., 2008). ©2008 by the American Astronomical Society)
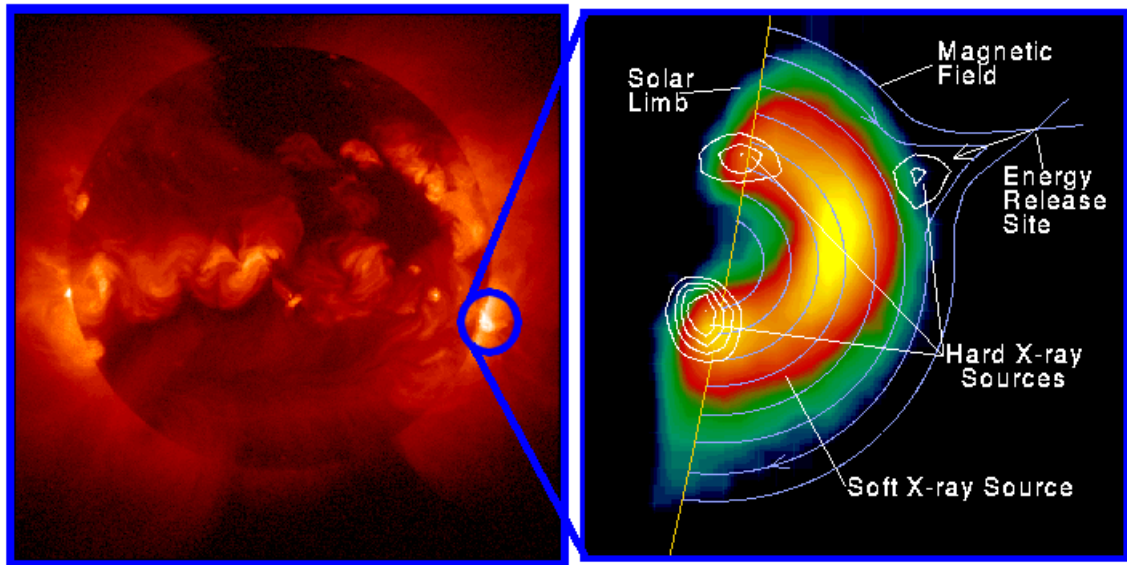
Figure 1.3: Yohkoh observations of the Masuda flare of 1992 January 13. Left, soft X-ray whole-Sun image; Right, magnified soft X-ray image with hard X-ray contours and a sketch of the common interpretation of the observed features. Yohkoh ("Sunbeam") was a Solar observatory spacecraft of the Institute of Space and Astronautical Science in Japan, in collaboration with space agencies in the U.S. and the U.K..

with the ambient plasma and magnetic field, generating solar flares. Those reaching the chromosphere (near the surface of the sun) produce footpoint emission. Those near the top of a loop in the corona produce looptop emission. Radiation across the electromagnetic spectrum from radio waves to gamma rays is observed.

Figure 1.3 is a soft X-ray (SXR) image from the whole Sun (left) with the Yohkoh spacecraft and a blowup of a flaring loop (right) with hard X-ray (HXR) contours overlaid on SXR intensity map. The loop body is bright in SXRs that are emitted by lines from highly ionized ions and free electrons. HXRs are observed at the looptop and footpoints. They are emitted via electron bremsstrahlung, a process in which electrons collide with ambient plasma, lose energy and subsequently emit radiation. The intensity of emission depends on the ambient plasma density. The

chromosphere, where the footpoints are, has a much higher plasma density than the corona, where the looptop is. Therefore, footpoint emission is usually much brighter than looptop emission (as seen from the denser contours at footpoints in Figure 1.3) and often overshadows the latter. As a result, looptop HXR sources are not as commonly detected. In the cases of limb flares that have a view angle from the side of the sun such that the footpoints and looptop are separated and occulted flares with occulted footpoints, looptop sources are more easily observed. The first observation of looptop HXR emission was in the notable Masuda flare (Masuda et al., 1994), a limb flare, 30 years ago. This discovery has important implications. Since magnetic reconnection, which is linked to the energy release process during solar flares, is supposed to happen high in the corona, existence of HXR-producing electrons in the high corona is evidence for particle acceleration associated with magnetic reconnection. Ever since the Masuda flare, more looptop sources have been detected with the improvement of detection sensitivity. A comprehensive analysis of 18 limbs flares exhibited 15 events with detectable looptop emission (Petrosian et al., 2002). It was therefore concluded that the detection of looptop emission is only a sensitivity problem, suggesting looptop sources are a common feature of all flares.
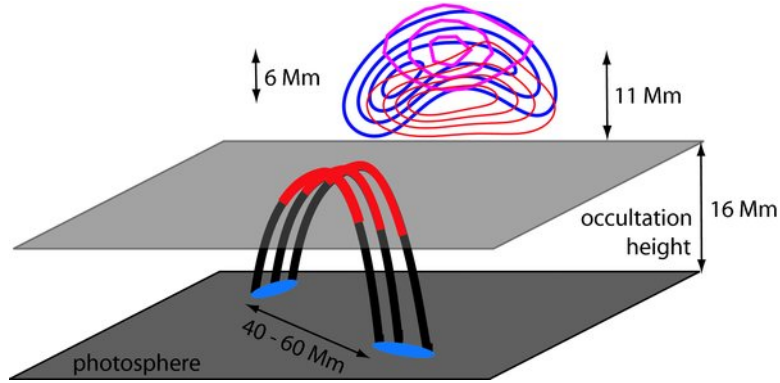
Figure 1.4: Cartoon of the 2007 December 31 flare. The dark gray plane represents the photosphere, and the lighter gray gives the occultation height of the RHESSI observations. The flare loops are shown in black (occulted part) and red (visible part). The contours of the HXR and microwave images are projected. Adapted with permission from Ref (Krucker et al., 2010). ©2010 by the American Astronomical Society)

1.2 Observations of X-ray Emission: Implication for Electron Transport

A very important implication from the observations of looptop emission is electron confinement in the corona. Figure 1.4 is an example of a looptop source, showing typical scales, from a recent intense (almost 10 times more than the Masuda flare) looptop X-ray emission. The sources were clearly observed because the solar disk was partially occulted when viewed from RHESSI, avoiding the saturation of the detector by bright footpoints at the disk. Using a system size of $\sim$10Mm, electrons producing HXRs at 50 keV take less than 0.1 sec to transit the flare loop and leave the source region. However, the decay time from the HXR time profile, which indicated the lifetime of the electrons at the source, was $\sim$30 sec (Krucker et al., 2010). That is over two orders of magnitude longer than the transit time. This

6

suggests that the energized electrons are trapped at the looptop. SXR counterparts of the HXRs were also observed at the looptop in this flare as in the Masuda flare. Many looptop X-ray observations share similar sizes and X-ray decay times, as reported from a statistical survey of 55 partially occulted flares (Krucker and Lin, 2008), implying electron confinement in the corona a common phenomenon in solar flares.

Recently, a systematic study of solar flares with both looptop and footpoint emissions found that the number of electrons required to explain observations is 2-8 times higher at the looptop than that at the footpoint (Simões and Kontar, 2013). This suggests electron accumulation at the looptop. Another systematic study of the relation between coronal and footpoint X-ray sources indicated that transport processes other than free-streaming of electrons from the corona towards the footpoints are involved (Battaglia and Benz, 2006). If there was only free-streaming, i.e., the same electron population produced the coronal and footpoint emission, the difference in photon spectral index between the two emission should be 2. Coronal and footpoint emissions are produced by thin-target and thick-target bremsstrahlung, respectively (because of the lower density in the corona and the higher density in the chromosphere). The study reported a difference in spectral index considerably greater than 2 in some events. This requires a filter effect in the propagation preferentially reducing the distribution at lower energies. Such a filter can be an electric field.

Evidence for free-propagation of energetic electrons, i.e., no interaction with the ambient plasma, was reported in previous time-of-flight (TOF) measurements of
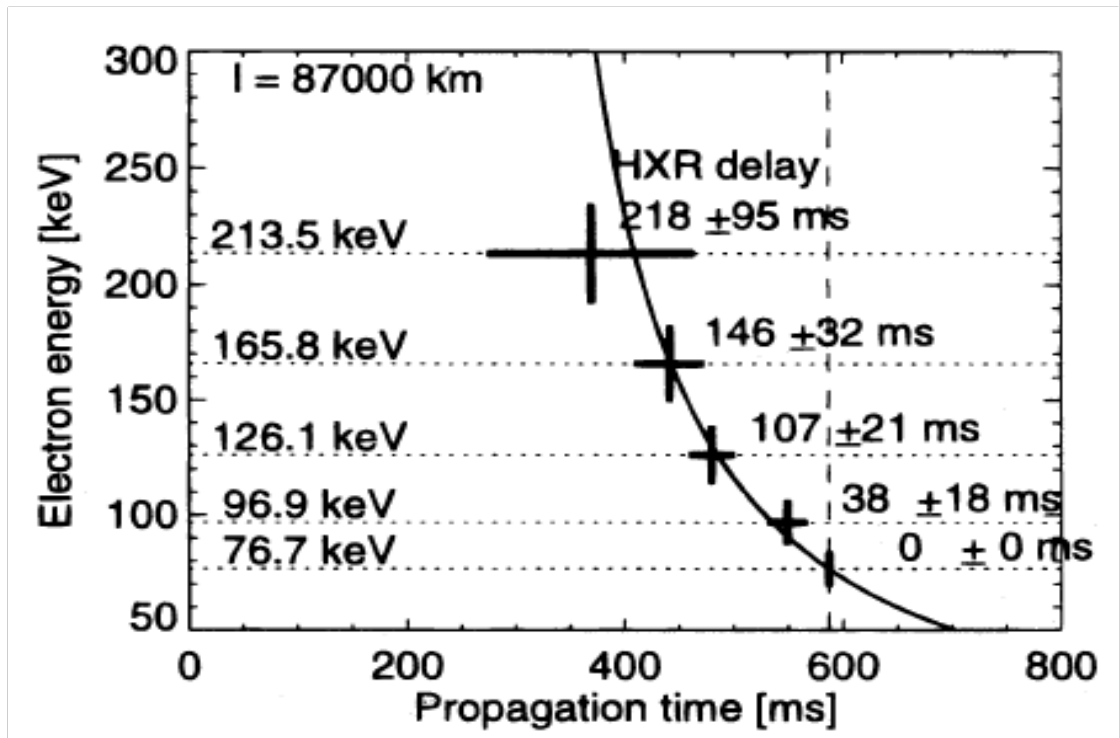
Figure 1.5: HXR pulse delays, from the Masuda flare, observed between five energy channels with electron energies indicated are fitted to a time-of-flight model. Adapted with permission from Ref (Aschwanden et al., 1996a). ©1996 by the American Astronomical Society.

HXR emission (Aschwanden et al., 1995, 1996b,a; Aschwanden and Schwartz, 1995). Time delays between HXRs at different energies indicate that lower energy electrons arrive at the chromosphere after higher energy ones as they freely stream down the flare loop from the corona. Figure 1.5 shows HXR pulse delays observed between five energy channels from the Masuda flare, fitted to the TOF model (Aschwanden et al., 1996a). They are consistent with the model, suggesting free-propagation of the HXR-producing electrons down the flare loop. A statistical correlation study of over 600 flares revealed a systematic time delay between lower (25-50 keV) and higher (50-100 keV) energy HXR emission (Aschwanden et al., 1995), supporting the free-streaming scenario of the energized electrons.

The transport of energetic electrons from the corona to the chromosphere is crucial to understanding energy release in flares. Transport effects can modify the energy distribution of the propagating electrons and hence the observed X-ray spectra, affecting the interpretation of acceleration models. An important question on electron transport is why some electrons appear to freely propagate while some are filtered or even trapped. The physics of this subject, however, remains poorly understood. In what follows, we attempt to understand this interesting subject.

1.3   Previous Work on Electron Transport

We first review some of the previous work on electron transport relevant to solar flares. Electron transport has been previously modeled as conduction mediated by classical collisions (Spitzer, 1962), convection at a subthermal characteristic speed
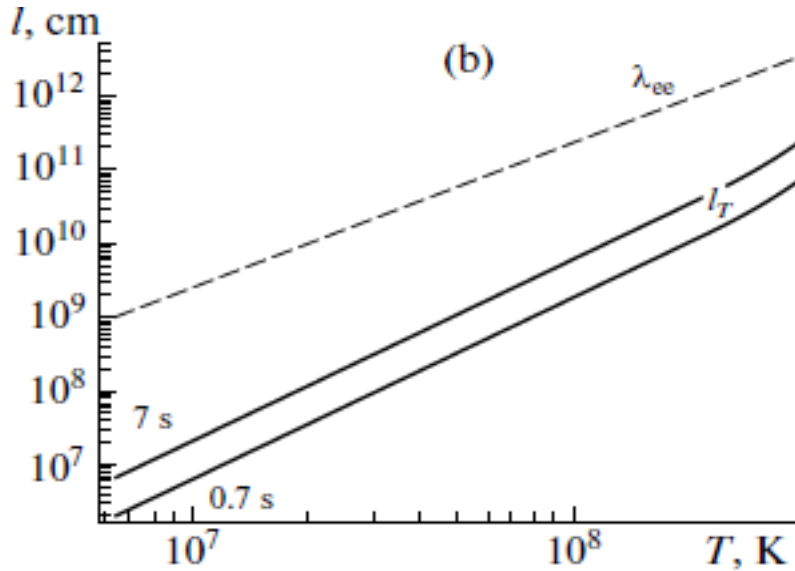
Figure 1.6: Plotted are the characteristic length scale l_T at two different times from a numerical calculation of heat conduction based on classical Coulomb collisions, and the thermal electron mean free path λ_{ee}. Adapted with permission from Ref (Oreshina and Somov, 2011). ©2011 by Springer.

observed in simulations of laser fusion studies (Manheimer and Klein, 1975), and turbulent transport limited by anomalous resistivity (Manheimer, 1977; Tsytovich, 1971), also called anomalous conduction.

Recent analytical and numerical studies of the transport of super-hot electron fluxes with energies greater than 10 keV show that the classical conduction model produced a heat flux significantly higher than the real energy fluxes reported from multi-wavelength observations of solar flares (Oreshina and Somov, 2011). This implies that processes other than classical Coulomb collisions between electrons and
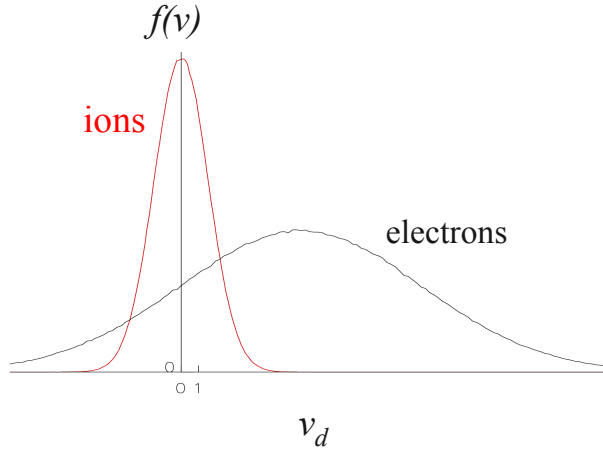
Figure 1.7: Ion and electron distributions unstable to ion acoustic instability. A relative drift v_d of electrons with respect to ions greater than the ion thermal speed, but less than the electron thermal speed, can excite ion acoustic waves.

ambient plasma needed to be considered as well. In Figure 1.6, the characteristic

length scale l_T corresponding to an e-fold change in temperature from their numerical

calculation is far less than the thermal electron mean free path λ_{ee}. This means that

the conduction model based on classical collisions is inapplicable to describe the flare

system under consideration. A kinetic (collisionless) model is required.

In the turbulent transport scenario, anomalous resistivity arises from electron

scattering by turbulent wave fields excited by instabilities involving the interaction

of energetic electrons and ambient plasma. One commonly considered mode is the

ion-acoustic instability (Manheimer, 1977; Tsytovich, 1971; Smith and Lilliequist,

1979; Levin and Melnikov, 1993). When accelerated electrons propagate outwards,

ambient electrons are drawn in as a return current. Their relative drift with ions

excites ion-acoustic waves (see Figure 1.7 for an example of ion and electron distri-

butions unstable to ion acoutic wave growth), which scatter the energetic electrons

11

and anomalously enhance resistivity (Manheimer, 1977). The heat flux carried by the energetic electrons is limited by the saturation of the instability due to ion trapping.

An anomalous conduction front that moved along the flare loop at the head of an expanding hot electron source was considered as a means to confine hot electrons for the production of HXRs (Smith and Lilliequist, 1979). The model, based on a 1D one-fluid code with a grid spacing of 100 km ($\sim 10^4$ ion inertial lengths), did not resolve ion inertial lengths, let alone capture processes occurring at electron scales. However, it was argued that the front propagates at approximately the ion acoustic speed c_s and, with some heuristic analysis, predicted that the front would become thinner than the grid spacing, although this was artificially disallowed to avoid numerical instability. Later, 1D electrostatic particle-in-cell (PIC) simulation that resolved the shortest electron scale, the Debye length, did not reveal a conduction front (McKean et al., 1990).

Recently, the existence of a thermal front, literally defined as a region that links plasmas in thermal nonequilibrium and sustains the temperature difference for longer than the electron free-streaming time, was studied in 1D electrostatic Vlasov simulations (Arber and Melnikov, 2009). Figure 1.8 shows the time evolution of the electron phase space near the contact between two temperature regions with the hot region representing a coronal electron source. In the top panel, the left and right sides are hot and cold electrons, respectively. From the top to the third panels, the front of the hot electrons propagated to the right, resembling thermal conduction. The authors therefore reported the formation of a temperature difference and

12
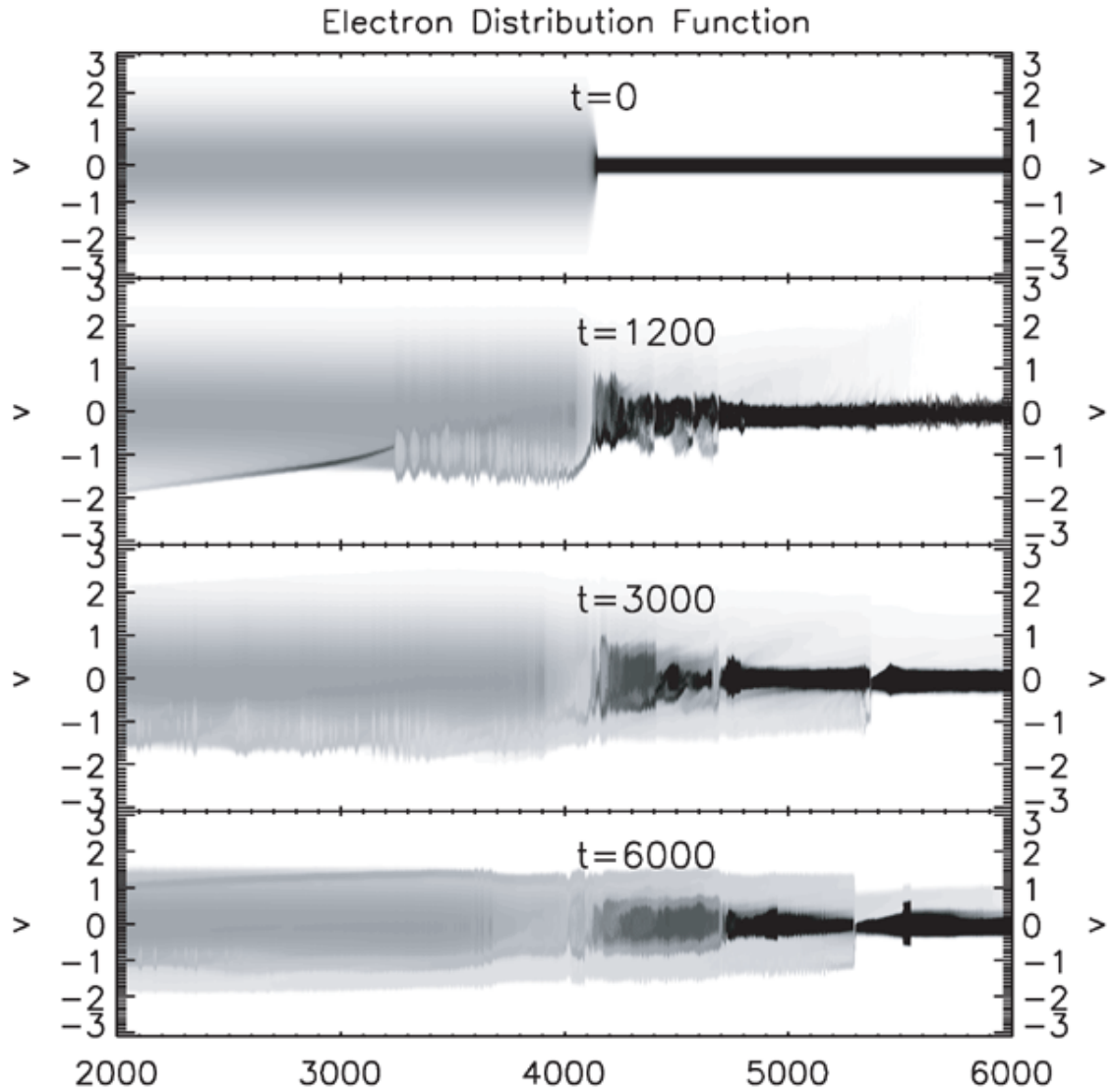
Figure 1.8: Time evolution of the electron phase space between the hot and cold electron populations in a 1D Vlasov simulation of coronal electron transport. Time is normalized to the inverse of the electron plasma frequency, space to the electron Debye length in the hot region and velocity to the hot electron thermal speed. Adapted with permission from Ref (Arber and Melnikov, 2009). ©2009 by the American Astronomical Society)

its propagation at a speed comparable to c_s. They identified the behavior as a conduction front. The physics of the responsible mechanism was not identified or investigated. The conduction front appeared to have moved backwards during the second half of the simulation (from the third to the bottom panels). Hence, there was likely no conduction during that period. We suggest, on the basis of the simulations and analysis in this thesis, that the propagating front is an ion acoustic shock and the temperature difference to be a result of shock heating due to its extremely sharp transition (see the sharp transition at x∼5300 in the bottom panel).

More recently, the transport of coronal energetic electrons was studied by electromagnetic PIC simulations (Li et al., 2012), to be presented in Chapter 3. It was shown that transport suppression began as the electrons propagate away from the acceleration site. The suppression is caused by the formation of a DL and associated potential barrier that reflected electrons back to the source. The DL model for electron confinement in the solar corona has not been presented previously. In what follows, we report results of this model from PIC simulations and analytic calculations.

Chapter 2

Double Layers

2.1   What is a Double Layer (DL)?
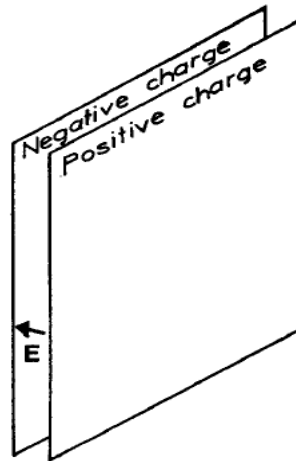
Figure 2.1: Schematic of a double layer as a capacitor. Adapted with permission from Ref (Block, 1978). ©1978 by D. Reidel Publishing Company, Dordrecht-Holland.

A DL is a localized region that sustains a potential drop in collisionless plasmas (Block, 1978; Raadu and Rasmussen, 1988; Singh et al., 1987). The potential drop comes from a nonlinear electrostatic electric field sandwiched between two adjacent layers of equal and opposite charges. It can be understood as a capacitor in a plasma (see Figure 2.1). Figure 2.2 shows the qualitative variation of the potential, electric field and charge density within a DL. The following conditions must be satisfied for a DL (Block, 1978):
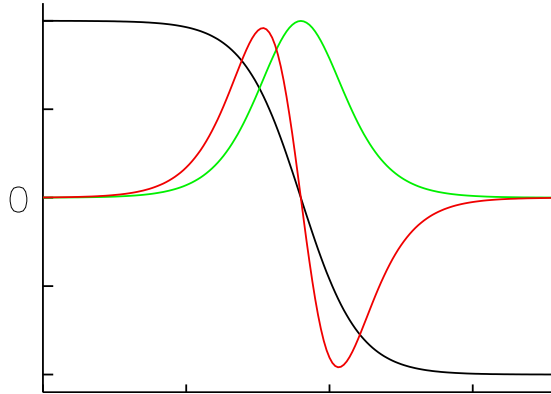
Figure 2.2: Schematic of a DL. A large-amplitude electric field E (green) is sandwiched between two layers of equal and opposite charge densities ρ (red). A net drop in the potential ϕ (black) results.
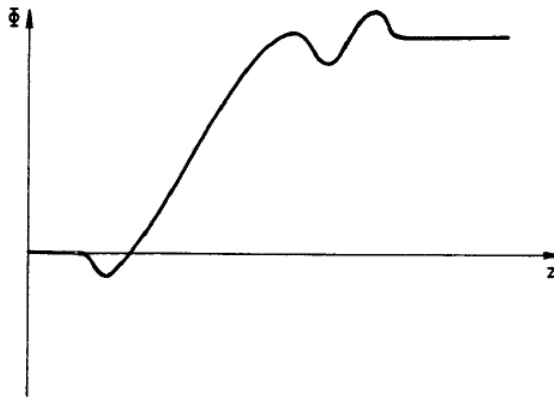
Figure 2.3: The potential profile of an non-ideal DL containing bumps and dips at its high and low potential side. Adapted with permission from Ref (Block, 1978). ©1978 by D. Reidel Publishing Company, Dordrecht-Holland.
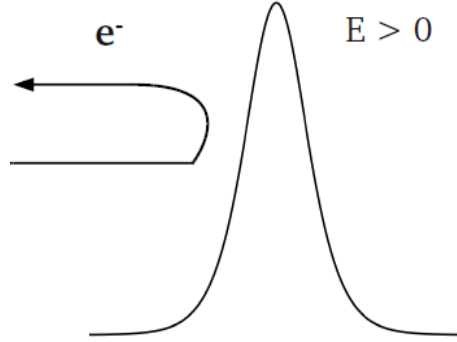
Figure 2.4: Schematic of an electron being reflected by a DL that has a positive electric field when approaching from its left.

(i) The electric field inside the DL is much stronger than outside.

(ii) Quasi-neutrality is locally violated within the layer.

(i) implies that, outside of the DL, the positive and negative charges almost cancel each other, leaving the electric field negligible. Given (ii), a DL occurs at scales of ~ 10 Debye lengths λ_{De}, where quasi-neutrality can be violated.

An ideal DL is a monopolar electric field, but more generally, a DL can be bipolar. Figure 2.3 shows an example of the potential profile of a non-ideal DL. Instead of a monotonic drop in potential ϕ, there can be dips or bumps at the low or high potential sides, but an overall potential drop ϕ_{DL} across the structure. ϕ_{DL} is the measure of the strength of a DL. DLs can be classified into strong and weak depending on whether ϕ_{DL} is much greater or comparable to the mean energy of the reflected particles on either side of the DL (Raadu and Rasmussen, 1988). In this work, the DLs observed have a potential comparable to the temperature of the

17

reflected hot electrons. They are weak DLs.

The potential drop of the DL can accelerate, decelerate and reflect particles entering from the two sides of the DL. For example, in Figure 2.4, electrons incoming from the left of a DL with a positive electric field, i.e., from the high potential side, will be decelerated (or reflected) if their kinetic energy is greater (or less) than ϕ_{DL}. In this work, it is the reflection of hot electrons by a DL that hinders their transport from the source region into the ambient plasma.

2.2   Previous Research on DLs

In this section, we highlight some previous theoretical studies on DLs.

Because of the nonlinear nature of DLs, it is in general difficult to analytically solve for time dependent solutions. For simplicity, earlier theories focused on steady state DLs. Steady state solutions of DLs may be derived self-consistently by solving the Poisson and time-independent Vlasov equations for ions and electrons in the DL frame. These can be regarded as an equilibrium solution of nonlinear waves described by the BGK method (Bernstein et al., 1957). This method constructed a class of stationary solutions by adding a trapped particle distribution given any potential profile and the remaining particle distributions. The particle distributions associated with a DL potential can be divided into four types: free and trapped (or reflected) ions and electrons. Figure 2.5 shows an example of the four particle types in ion and electron phase space for a given DL potential. For strong DLs, all four types of particle distributions are required. For weak DLs, three types suffice (Raadu
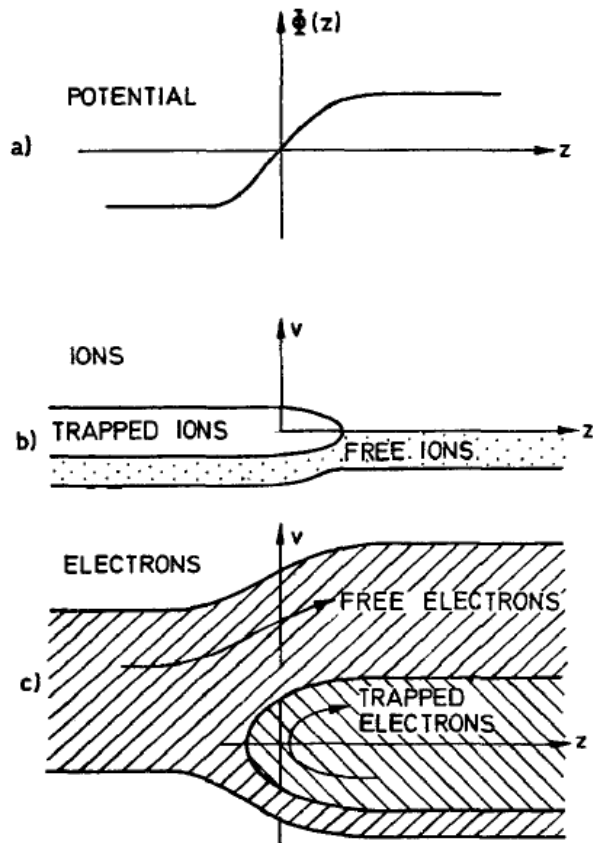
Figure 2.5: (a) The potential profile of a DL. Phase space for trapped and free (b) ions and (c) electrons. Adapted with permission from Ref (Block, 1978). ©1978 by D. Reidel Publishing Company, Dordrecht-Holland.

and Rasmussen, 1988). In this work, we observe weak DLs and three types of particle distributions: free and trapped electrons, and free ions. Later, following the BGK method, it was showed that a fourth particle velocity distribution can be uniquely determined if three of the four velocity distributions and a potential variation (of a DL) are specified (Knorr and Goertz, 1974). Thus, they demonstrated the existence of a BGK solution, showing that an arbitrary potential profile can be constructed if the right trapped particle distribution is added.

In addition to the existence of stationary DLs, their stability was also in question. Research was directed to study the general stability of DLs. Knorr and Goertz (1974) proved that the uniform plasmas on either side of the stationery DL solutions is Penrose stable, i.e., no electrostatic current-driven instabilities. However, the proof was limited to the particular velocity distribution chosen and incomplete because modes due to density inhomogeneity were not considered. Wahlberg (1979) showed that local Penrose-stability was in general insufficient for global stability due to the existence of linearly unstable trapped Langmuir modes that may exist within a DL. This led to a stability requirement that the thickness of the DL must be smaller than a critical value. It was shown that very weak DLs were linearly stable to longitudinal 1D perturbations, but unstable to transverse perturbations (Schamel, 1983).

Later, the time dependence of DLs was investigated. The dynamics of weak DLs can in some cases be described by the modified Korteweg-de Vries equation with a perturbative approach for small-amplitude waves (Torven, 1981; Raadu and Chanteur, 1986; Bharuthram and Shukla, 1986). More generally, numerical simu-

lations have been used to understand the time dependent and nonlinear behavior of DLs. The dynamics of DLs, including their generation and decay, were studied. We review some of the key results in the following. Extensive reviews are available (Raadu and Rasmussen, 1988; Raadu, 1989; Singh et al., 1987).

2.2.1 Generation Mechanisms
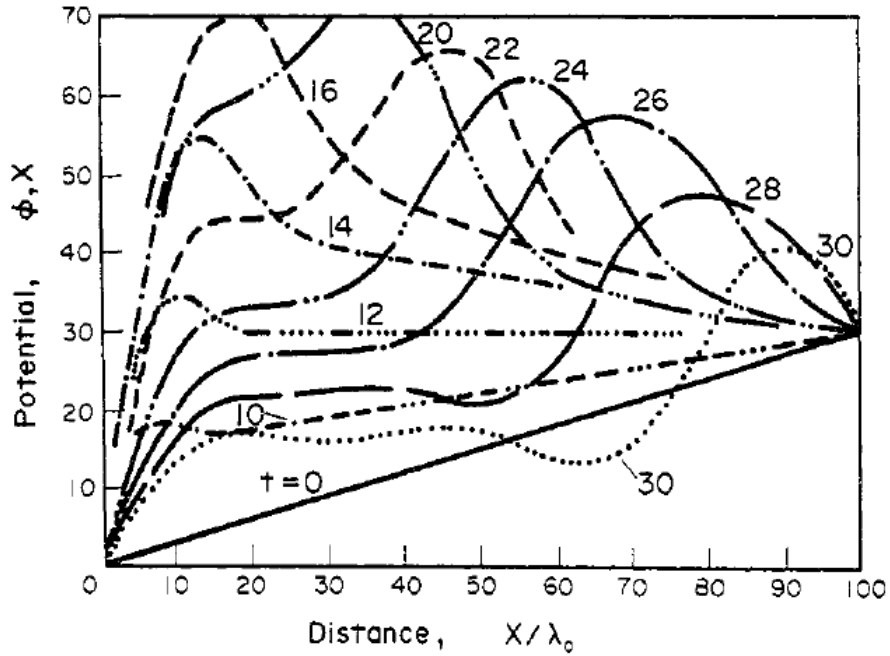
Figure 2.6: Temporal evolution of the potential profile of a DL driven by an applied potential. Adapted with permission from Ref (Singh, 1982). ©1982 by Institute of Physics and Pergamon Press Ltd.

Generation mechanisms of DLs include a current and an applied potential. Since DL formation is basically creating a potential drop, applying a potential across a collisionless plasma system may drive a DL along with other plasma processes. The external potential applied in numerical simulations (Goertz and Joyce, 1975; Joyce

and Hubbard, 1978; Singh, 1982; Singh and Schunk, 1982) and labortory experiments (Torvén and Babić, 1975; Quon and Wong, 1976; Coakley and Hershkowitz, 1979; Iizuka et al., 1985) ranged from 10 to 100 times the electron temperature. Strong DLs were typically observed and the formation was cyclic. It was argued that the cause of cyclic formation is the difference in the ion and electron time scales (Singh, 1982; Singh and Schunk, 1982). Initially, electrons dominated the dynamics in response to the applied potential. An electron current was accelerated and the result was charge separation in the cathode (the low potential boundary), triggering a large positive potential pulse. Figure 2.6 shows the temporal evolution of the potential profile. The initial large potential pulse near the cathode evolved into a DL, which propagated towards the anode. Ions were accelerated by the DL, producing counterstreaming ion beams. While the applied potential drove an ion outflux from the anode, as the DL moved the ion flux (current) reversed to influx. As the ion current through the DL recovered, so did the electron current. The system returned to nearly its original state. At the cathode, fluctuations of the potential associated with the current restoration triggered the formation of a new DL. The cycle repeated.

In the case of injecting a current, DLs develop in the nonlinear stage of current-driven instabilities such as the Buneman, ion-acoustic, ion-cyclotron and electron-acoustic instabilities (Sato and Okuda, 1980; Ishiguro et al., 1997; Lee et al., 2008). For instance, 1D Vlasov simulations with an electron beam drifting at higher than the electron thermal speed reported the formation of a strong DL from the Buneman instability (Singh et al., 1985). As can be seen in Figure 2.7, the DL evolved on a
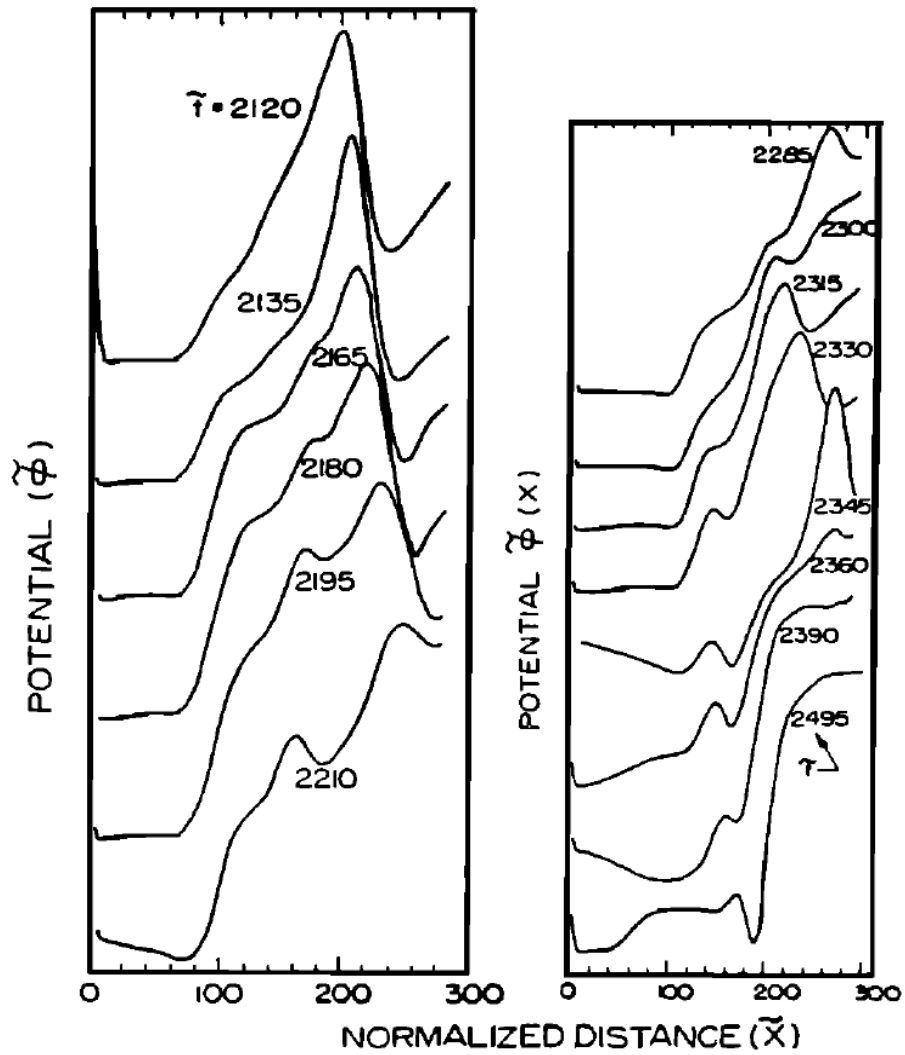
Figure 2.7: Temporal evolution of the potential profile of a DL driven by the Buneman instability. It was never in a stationary state. Adapted with permission from Ref (Singh et al., 1985). ©1985 by the American Geophyical Union.

time scale of a few electron plasma periods, and was therefore not in a stationary state. Similarly, weak DLs were generated from the ion-acoustic (IA) instability. It was suggested in 1D particle simulations that enhanced anomalous resistivity driven by the IA instability caused the formation of a DL (termed as an IA DL) (Sato and Okuda, 1980). Instead of having a monotonic potential profile (ϕ in Figure 2.2) commonly seen for strong DLs, weak DLs had a dip in the low potential side. It was proposed that the existence of such a dip was responsible for the formation of IA DLs (Hasegawa and Sato, 1982). The potential dip reflected electrons from the electron current that drove the IA instability and left the other side of the dip ion-rich, which resulted in charge separation and therefore a DL. A combination of 1D and 2D particle simulations and analytic work which used a Korteweg-de Vries equation modified to include kinetic effects of electron reflection supported this scenario (Nishihara et al., 1982). 1D Vlasov simulations and an adiabatic theory assuming equilibrium of the electrons with the potential dip showed that the DL amplified by exchanging momentum with the reflected electrons (Chanteur et al., 1983). The adiabatic theory agreed well with the simulation results. It broke down when ion trapping became evident.

The DL observed in our simulations is generated by imposing a large field-aligned temperature jump in the initial state which results in strong currents that drive the DL. Details of the generation are described in Chapter 3.

2.2.2 Decay Mechanisms

Decay of DLs was also observed in time dependent studies. 1D PIC simulations of systems driven by a subthermal electron current showed that ion trapping in the potential dip of a DL was associated with its decay (Barnes et al., 1985). The trapping of ions slowed down the movement of the DL structure as the trapped ions added an inertial drag to it (Chanteur et al., 1983). It was argued that such slowing down led to the decay of the DL (Barnes et al., 1985). Figure 2.8 shows time series plots of the ion phase space (left) and potential profile (right) for a simulation driven by the IA instability. A potential dip/well gradually developed and ions were trapped inside. As the dip amplified, a net potential drop eventually appeared at the right of the dip at the time marked by an asterisk, indicating the formation of a DL. In the mean time, ion trapping resulted in the development of an ion hole in the phase space. The DL structure as well as the ion hole gradually slowed down and finally reached zero propagation speed indicated by a black arrow. The potential drop decayed. IA solitons were emitted and propagated downstream (i.e., towards the high potential side).

1D PIC simulations with an applied potential reported that a DL decayed as a result of the propagation of a train of IA solitons, which developed from the DL structure, across the DL width (Sato and Okuda, 1981). Figure 2.9 shows the time evolution of the potential profile as a potential drop developed (left column) and then spiky wave trains (right column), identified as IA solitons, were emitted. They moved downstream (i.e., towards the high potential side) and then the potential
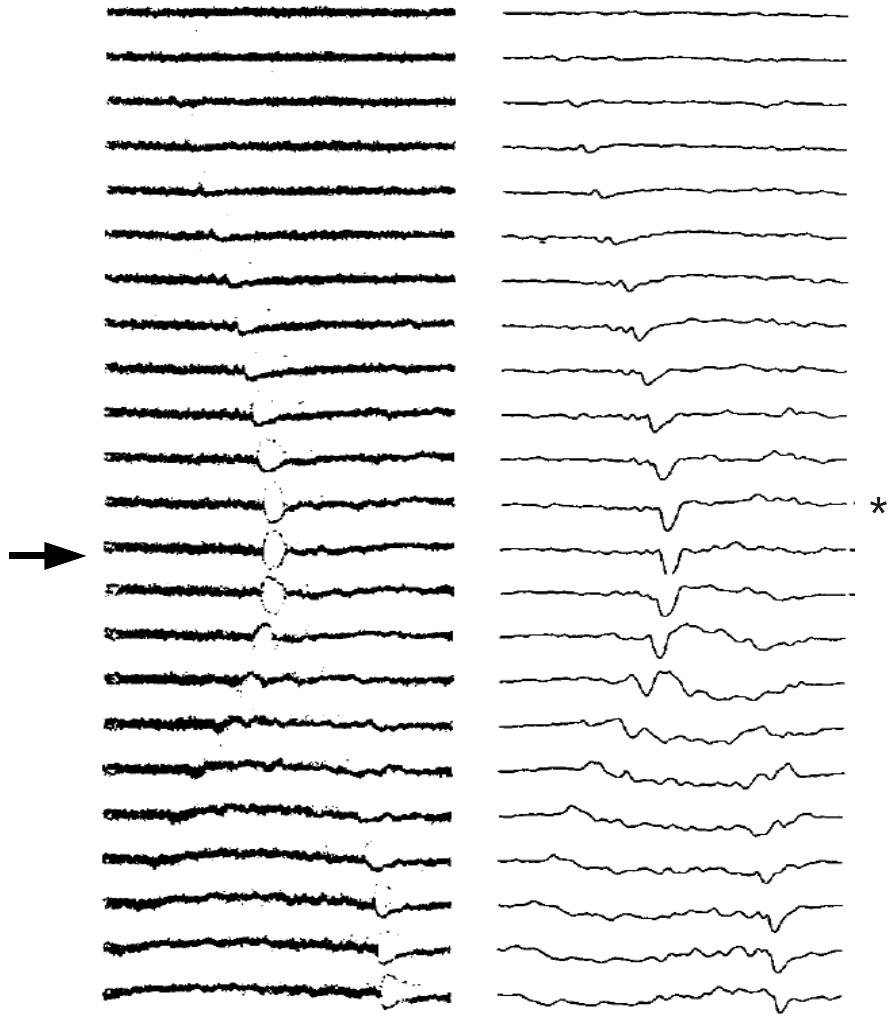
Figure 2.8: Time series plots of the ion phase space (left) and potential profile (right) from a 1D simulation. Adapted with permission from Ref (Barnes et al., 1985). ©1985 by the American Institute of Physics.
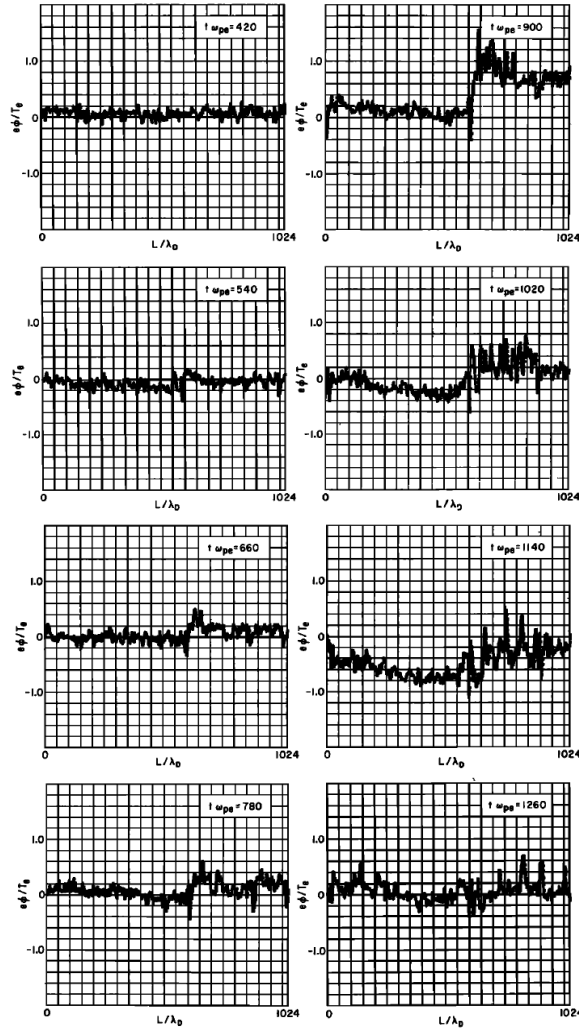
Figure 2.9: The potential profile during the formation (left column) and then decay of a DL due to emission and propagation of IA solitons towards the high potential side of the DL. Adapted with permission from Ref (Sato and Okuda, 1981). ©1981 by the American Geophyical Union.

drop decayed. Only very limited work exists on the saturation of DLs.

In this work, the DL saturates as its potential drop is large enough to accelerate ions to supersonic speeds to drive an IA shock (Li et al., 2013a). The shock stabilizes the Buneman instability that is the driver of the DL and saturates the DL. This will be presented in Chapter 4.

2.3   Applications to Space and Astrophysical Plasmas

We review some applications of DLs to space and astrophysical plasmas. Much research interest on DLs has focused on their ability to directly accelerate particles in auroral (ionospheric and magnetospheric) and astrophysical plasmas (Singh et al., 1987). For particle acceleration, the potential across the DL is usually maintained by some external energy source. A DL theory was proposed for the production of high-energy particles during the impulsive phase of solar flares (Hasan and Ter Haar, 1978). A series of weak DLs is believed to be responsible for the acceleration of kilovolt electrons in the aurora (Kan et al., 1979; Borovsky, 1992). A field-aligned electron current, usually involving the Birkeland current, is assumed to provide the energy source for the DLs (Akasofu, 1977). An analytical model of diffusive acceleration of electrons in the auroal plasma due to the interaction with weak DLs was developed (Lotko, 1986).

A succession of many weak DLs, occurring from the corona to the Earth, was considered as the source of the interplanetary potential difference in exospheric models of the solar wind expansion (Lacombe et al., 2002). The potential decelerated

fast moving electrons and accelerated protons in the solar wind to maintain equal flux of both species during the solar wind expansion.

DLs were also invoked in the outer planets. Particle acceleration by DLs was modeled and applied to Jupiter's ionosphere to explain observations of energetic electrons (of greater than 0.15 MeV) by the Pioneer 10 and 11 spacecrafts (Shawhan, 1976). It was argued that a DL may be present in the accretion column of a neutron star in a binary system, and may dominate in the deceleration of the accreting ions over other processes such as a collionless shock (Williams et al., 1986).

2.4   Observations in Space Plasmas

The first observations of weak DLs in the Earth magnetosphere, in the high altitude auroral zone, were made with a three-component electric field probe on the S3-3 satellite (Temerin et al., 1982). In the same region, weak DLs were reported to occur frequently (Mozer et al., 1985). They have parallel electric fields directed upward and many contain sufficient potential to account for the parallel acceleration of upgoing ion beams and auroal electrons. Figure 2.10 illustrates observed features associated with DLs. Three bars plotted above the top panel indicate times of DL events of which the black solid regions represent known occurrence and the cross-hatched regions represent probable presence. Evidence for ion acceleration by DLs is seen by the factor of 100 increases in the upgoing ion flux (second panel from the bottom) during the two DL events. Signatures of accelerated electrons are present in the loss cones (decrease in electron density, second panel) and fluxes (bottom panel)
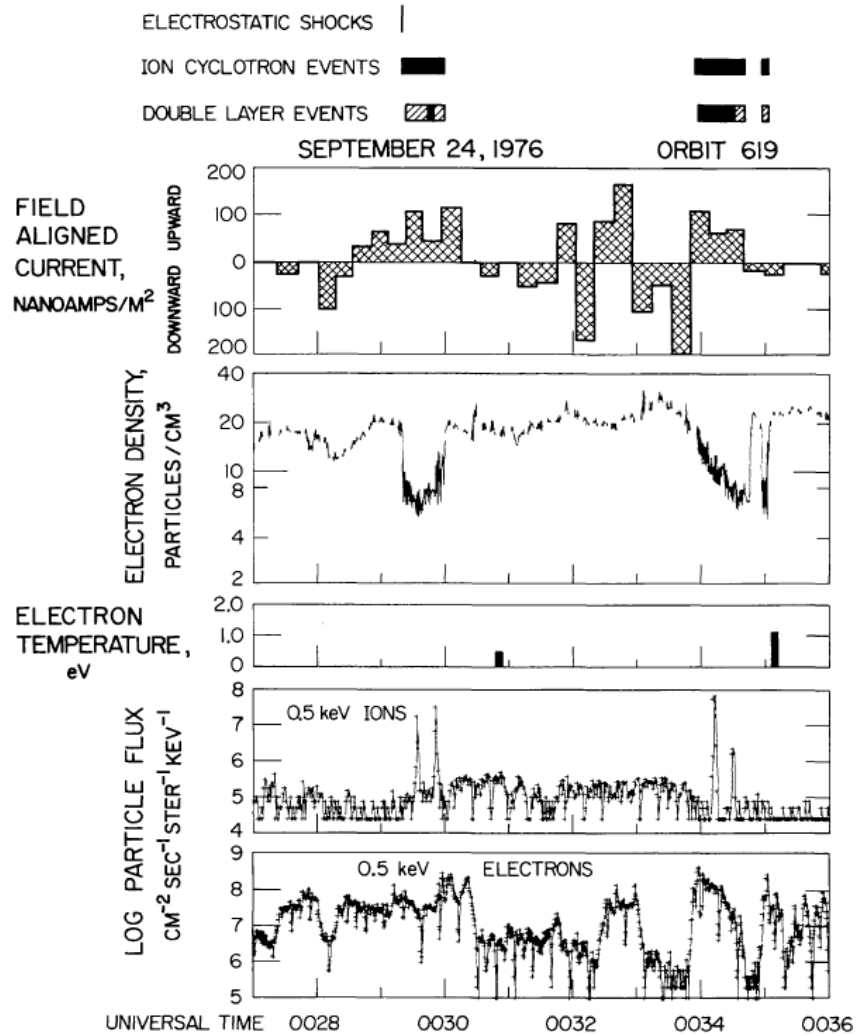
Figure 2.10: Field-alligned currents and particle fluxes measured near regions containing DLs, in the magnetosphere by the S3-3 satellite. Adapted with permission from Ref (Mozer et al., 1985). ©1985 by D. Reidel Publishing Company.

of electrons. In the Earth's plasma sheet, a high number of weak DLs are detected by the THEMIS (Angelopoulos, 2008) spacecraft during periods of high magnetic activity, implying that DLs may be a frequent occurrence in such situations (Ergun et al., 2009). Figure 2.11 is an example of one of the DLs observed in the current sheet during periods of strong fluctuations in the magnetic and electric fields. A turbulent region of electron phase space holes (bipolar electric field signatures) were seen adjacent to the DL, indicating presence of electron beams.

In the solar wind, weak DLs, with a smaller amplitude than those in the auroal regions, were first observed by the WIND spacecraft near the Lagrange point L_1 (Mangeney et al., 1999). Figure 2.12 shows an example of the observed isolated DLs, which have a small jump in the electrostatic potential of a few mV. When compared to the solar wind electron temperature of $\sim$10 eV (Newbury et al., 1998), the potential jump is $q\Delta V/k_B T_e \simeq 3\times10^{-4}$.

DLs were also inferred in the outer planets, including the magnetospheres of Jupiter (Hess et al., 2009) and Saturn (Gurnett and Pryor, 2012).
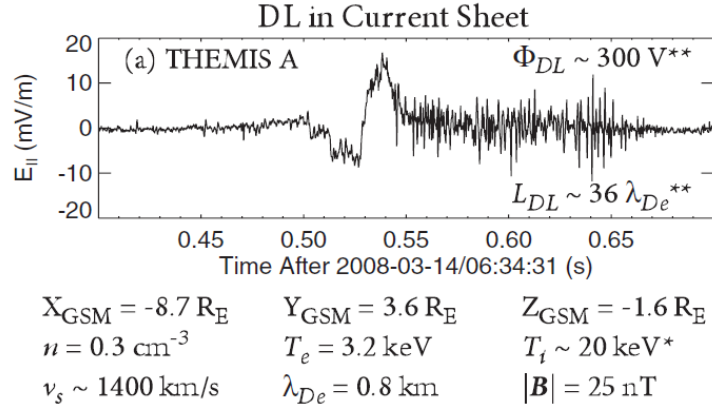
Figure 2.11: The parallel electric field data from the THEMIS satellites showing a DL (the large-amplitude positive peak) and a region of turbulence to its right. Properties of the DL are on the plot. Plasma conditions and the location are below the plot. Value marked with * are estimates and with ** assume that the DL moves at the ion acoustic speed v_s. Adapted with permission from Ref (Ergun et al., 2009). ©2009 by the American Physical Society.
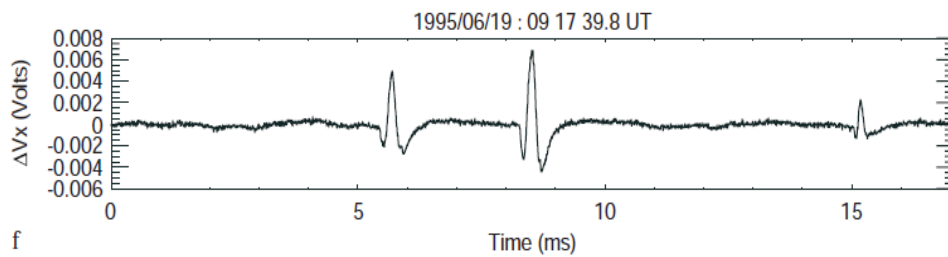
Figure 2.12: A typical wave form of isolated weak DLs observed by the WIND spacecraft. Shown is the electric potential ΔV_x. Adapted with permission from Ref (Mangeney et al., 1999). ©1999 by the European Geophysical Society.

Chapter 3

Suppression of Electron Transport by DLs and DL Generation

To gain a better understanding of the problem of energetic electron transport from the corona to the chromosphere, an important question that must be answered is whether thermal conduction is suppressed when the accelerated electrons start to propagate into the immediate surrounding plasma. Our goal in this chapter is to answer this basic question.

To study the physics at the electron scale and the nonlinear aspects of the problem, we perform a PIC simulation. We observe that the transport of energetic electrons is suppressed by a double layer that occurs at the shortest scale in a plasma, the Debye length λ_{De}. In what follows, we describe the setup of the simulation and present key results.

3.1 Simulation Setup for a Coronal Electron Source
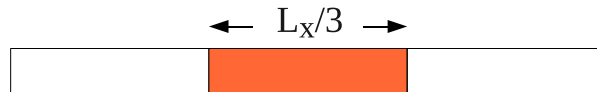
Figure 3.1: Schematic of the initial simulation setup.

We are exploring the problem of energetic electron transport from the corona to the chromosphere by a two-dimensional electromagnetic PIC simulation using the p3d code (Zeiler et al., 2002). A rectangular domain (Figure 3.1) represents

a symmetric local segment of a flare loop centered at the loop-top where a very hot electron source is located. The long direction, x, is along the loop axis and an initial uniform background magnetic field B_0 is applied in that direction. The short direction, y, is mainly for data averaging to produce smoother data in x. The initial density n_0 is uniform. A third of the electrons, centered in the domain, have higher initial parallel temperature $T_{h0,\parallel}$ than the rest[1]. It represents a pre-accelerated hot looptop source. Higher $T_{h0,\parallel}$ is used because parallel transport is of more interest since it dominates over perpendicular transport in the presence of a strong magnetic field, which is the case for a coronal flare loop. Electrons are initially modeled by bi-Maxwellian distributions and the ions by a Maxwellian distribution. We consider it to be more natural that the hot population not have a preferred direction of propagation, so the simulated energetic electrons are not beamed in the initial state. We note that SXR counterparts of HXRs are observed in the high corona (Masuda et al., 1994; Krucker et al., 2010). SXR spectra can be well fit by a Maxwellian distribution (Masuda et al., 2000; Tsuneta et al., 1997) while HXR spectra are usually fit by a combination of a thermal and a beam distribution. The use of Maxwellian distributions in our simulation setup is therefore consistent with thermal sources in coronal SXR and HXR observations. However, the qualitative features of our results are not expected to be sensitive to the form of the hot electron

---

[1]Using an anisotropic initial distribution for the hot electrons is not expected to affect the results because the setup is stable to possible instabilities in quasi-linear theory (Melrose, 1980), and the electron firehose instability (Hollweg and Völk, 1970) which may be excited by higher parallel than perpendicular electron pressures.

distribution (further discussed in Section 7.2).

Temperatures are normalized to $m_i c_A^2$, where m_i is ion mass and $c_A = B_0/(4\pi m_i n_0)^{1/2}$ is the Alfvén speed. In the hot electron region, $T_{h0,\parallel}=0.5$ is used. Hot electrons have unity plasma beta β (ratio of plasma pressure to magnetic pressure) in the parallel direction. Using unity β for hot electrons is consistent with recent coronal flare observations (Krucker et al., 2010). Outside of the hot electron region, the ambient (cold) electron temperature T_{c0} is 0.1, as are both the perpendicular temperatures throughout the domain and the ion temperature. We will drop "$\parallel$" in $T_{0,\parallel}$, and use T_e to represent the parallel electron temperature in general from here on for simplicity.

The size of the simulations is $L_x \times L_y = 655.36 \times 2.56\ d_e^2$ with a cell size of $0.02 \times 0.02\ d_e^2$. There are 400 particles per cell. $d_e = c/\omega_{pe}$ is the electron inertial length, where $\omega_{pe} = (4\pi n_0 e^2/m_e)^{1/2}$ is the electron plasma frequency. For $T_h = 5$ keV and n=10^9 cm^{-3}, which are typical of coronal thermal X-ray sources, $L_x \sim 100$m, which is of course far smaller than a realistic flare loop. Thermal speeds are defined as $v_{tx} = (2T_x/m_x)^{1/2}$. The Debye length based on the initial hot electron temperature is $\lambda_{De} = v_{te0,h}/\omega_{pe} = 0.1\ d_e$. We will use d_e as the unit of length, but it can be conveniently converted to λ_{De}. Time is normalized to ω_{pe}^{-1}. A mass ratio m_e/m_i of 1/100 and speed of light c/c_A of 100 are used. Electric fields are normalized to $E_0 = c_A B_0/c$. The system is periodic in both directions. Because of the periodic boundaries, the simulations are evolved for less than the electron transit time of the domain at $1.5v_{h0}$, so the majority of hot electrons will not reach a boundary during a run.
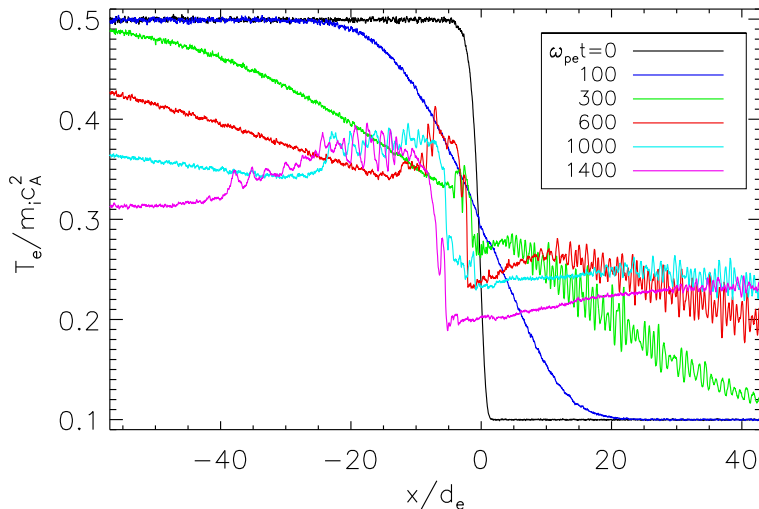
Figure 3.2: Evolution of electron temperature T_e parallel to the local magnetic field near the transition between hot and cold electrons, at x= $0d_e$. We begin with two electrons populations in contact (black) and let them evolve. The initial gradient becomes a smooth diffusive profile at ω_{pe}t=100 (blue). The smooth transition is then interrupted by a jump which signifies transport suppression from the high to low T_e sides.

3.2   A Jump in Electron Temperature

The primary drive of the system is the contact of hot electrons with cold electrons, so the dynamics starts in the region of contact. Since this is a symmetric system, it suffices to study either side of the contact. We choose the right side, where hot electrons propagate outwards with positive velocities. The figures are averaged in y since there is no significant variation in that direction. Fig. 3.2 shows the time evolution of electron temperature in the region where the hot and cold electrons come into contact. The initial profile (black) represents a high temperature region decreasing to a low temperature region through a narrow transition that has a

36

length scale of several d_e's. We do not expect the results to be sensitive to this transition scale since we find that the DL develops from a streaming instability after the temperature discontinuity has broadened. Over a short period of time ($\sim$100 ω_{pe}^{-1}, blue), the transition broadens as the hot electrons free-stream into the cold electron region. If free-streaming were to continue, we would expect the profile to continue to broaden due to the mixing of the two populations. However, a small jump develops (see ω_{pe}t=300) within the smooth transition, meaning that the escape of hot electrons by free-streaming is inhibited. Over time, the jump grows in size and significantly suppresses mixing due to free-streaming. As a result, the previously smooth transition is converted into a distinctive jump across two separate temperature regions. This indicates that the transport of hot electrons into the surrounding plasma is being suppressed. Other features of Fig. 3.2 include Langmuir waves propagating in the cold electron side (see e.g., the wiggles on the right side of the curve at ω_{pe}t=300) that are excited by the bump-on-tail instability as hot electrons free-stream into that region. Beam modes are excited on the hot electron side (see, e.g., longer scale waves on top of the curve at ω_{pe}t=1400) by the electron-electron streaming instability as cold electron beams that are accelerated by a DL enter the hot side and interact with the hot electrons.
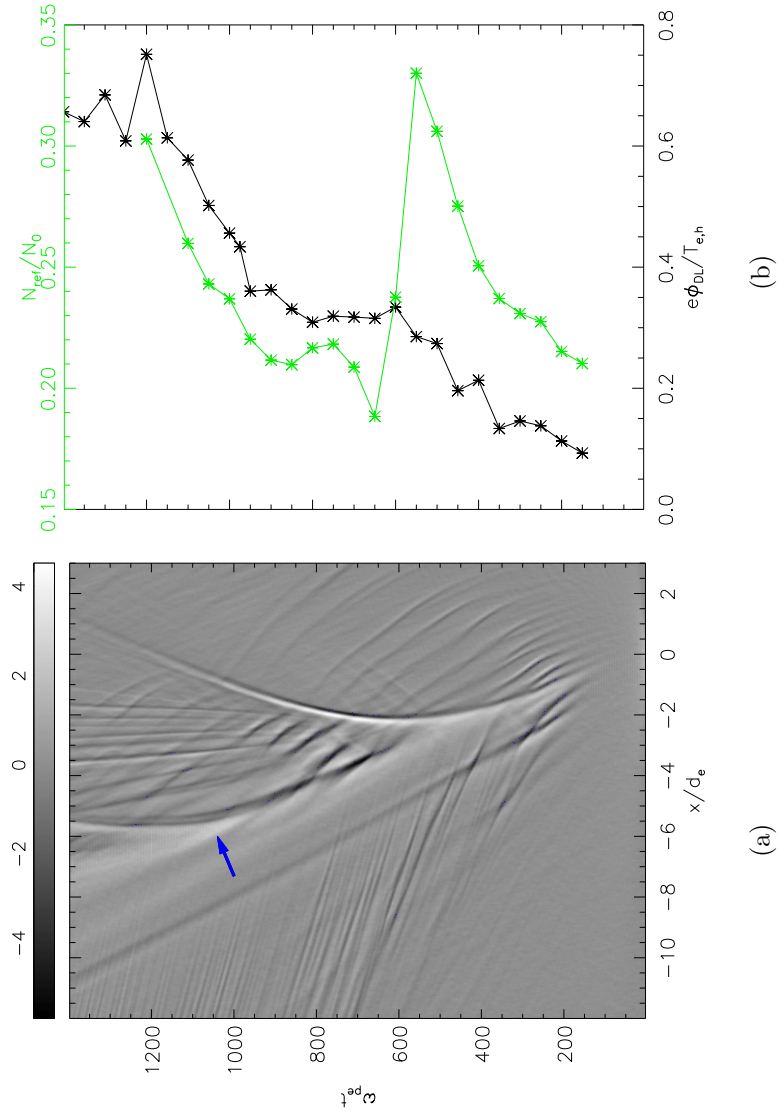
Figure 3.3: Evolution of (a) E_x, the parallel electric field and (b) $e\phi_{DL}/T_{e,h}$ (black), the electric potential jump across the DL normalized to the instantaneous hot electron temperature at the center of the hot region, overlaid with N_{ref}/N_0 (green), the fraction of return current electrons reflected at the foot of the DL divided by the total initial electron number. The DL is indicated by a blue arrow.

3.3 DL Evolution and Strength

The heat flux suppression comes from a DL that arises within the transition region. Figure 3.3(a) shows the time history of the electric field parallel to the local magnetic field, E_x, and 3.3(b) the time evolution of the electric potential jump across the DL normalized to the instantaneous hot electron temperature measured at the center of the hot region, $e\phi_{DL}/T_{e,h}$. $T_{e,h}$ in $e\phi_{DL}/T_{e,h}$ thus represents the core temperature of the hot electron population. $T_{e,h}$ drops over time as can be seen on the left side of Fig. 3.2 because hot electrons continuously leak out. We normalize the potential jump of the DL to $T_{e,h}$ to more accurately reflect the suppression strength of the DL on the hot electrons that remain in the source region at any particular time. Also shown in Fig. 3.3(b) is the fraction of return current electrons that are reflected at the foot of the DL, normalized to the initial total electron number, N_{ref}/N_0. The reflection mechanism and the reason for its importance are discussed later. E_x is averaged over an electron plasma period to eliminate initial fluctuations in the contact region that decay over time. The DL emerges at $\omega_{pe}t\sim100$ around x=0. At $\omega_{pe}t\sim550$, it emits a large amplitude shock that moves in the positive x direction. The DL, indicated by a blue arrow, is the white region in Fig. 3.3(a) that slowly drifts in the negative x direction. The DL is constantly evolving over the entire course of the simulation. At $\omega_{pe}t=1200$, it reaches its maximum amplitude and extends over a scale of 4 d_e, centered at x$\sim$ -6d_e. Fig. 3.4 is a cut of Fig. 3.3(a) at this time in a blowup around its location. Shown are E_x (blue), the electric potential normalized to the core hot electron temperature $e\phi/T_{e,h}$ (black) and the electron
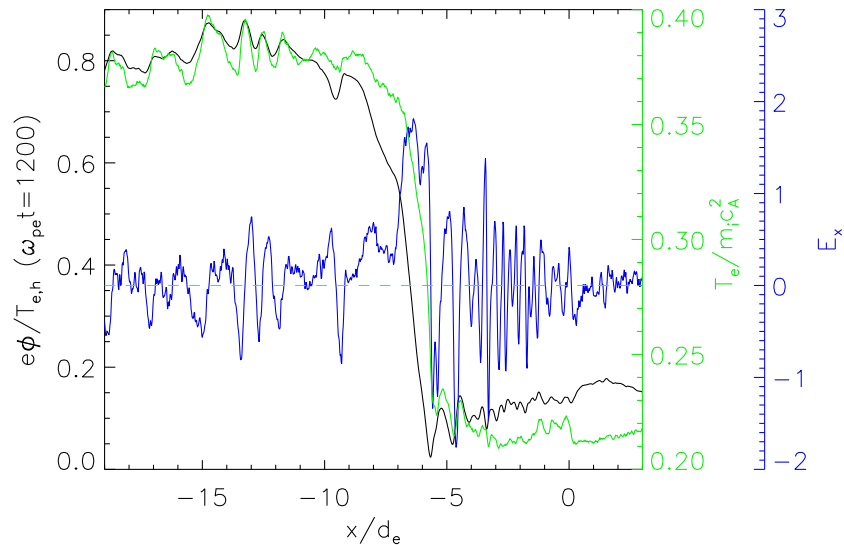
Figure 3.4: $e\phi/T_{e,h}$ (black) and T_e (green), overlaid with E_x (blue) and the zero E_x position (dotted cyan), at $\omega_{pe}t=1200$. The DL is characterized by a monotonic drop in the potential. The potential barrier suppresses the transport of hot electrons and results in a drop in T_e across the DL.

temperature T_e (green). E_x has a large positive peak at x$\sim$ -6d_e that causes a large potential drop that reflects hot electrons and produces a sharp drop in the electron temperature. We define the strength of the DL by its potential jump $e\phi_{DL}$ which is calculated as follows. To the left of the DL in Fig. 3.4, the potential increases, oscillates and eventually reaches a fairly constant value (near x$\sim$ -13d_e), the high end value. To the right of the DL, the potential drops and oscillates about a roughly constant value (near x$\sim$ -5d_e), the low end value. $e\phi_{DL}$ is the difference between the high and low end values and is shown as a function of time (black) in Fig. 3.3(b). $e\phi_{DL}/T_{e,h}$ is a measure of the suppression capability of the DL on the hot electron transport. If the DL is large enough such that $e\phi_{DL}/T_{e,h} \sim 1$, the thermal bulk of the hot electrons will be reflected by the potential barrier of the DL. This will imply
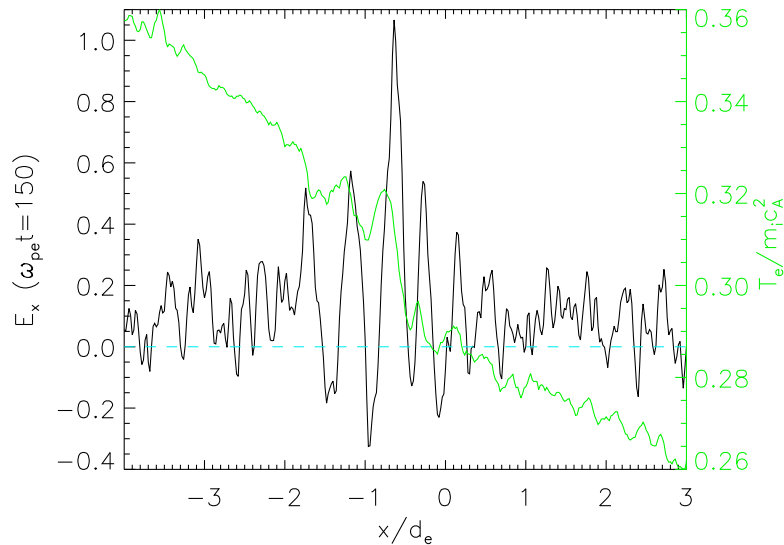
Figure 3.5: The electric field E_x at $\omega_{pe}t{=}150$, overlaid with T_e (green). The large amplitude wave that forms around x<∼0 arises from an ion/return-current-electron streaming instability.

a significant reduction of the electron heat flux as well.

Note also in Fig. 3.4 that the DL is not merely a unipolar electric field. It has a small negative leg between x= -6 and -5d_e, on the low T_e side. While the bigger positive part suppresses streaming hot electrons coming from the left, the negative leg can reflect cold electrons coming from the right (low T_e side). The reflection of these electrons is the drive mechanism of the DL, which we now discuss. Fig. 3.5 is a cut of Fig. 3.3 (a) at $\omega_{pe}t{=}150$, shortly after the DL emergence. Multiple peaks in E_x develop in the T_e transition region. In the linear regime ($\omega_{pe}t{<}150$), these waves have small amplitude, comparable to the background fluctuations. They gradually grow into large-amplitude nonlinear structures at later times. The peak which has the largest amplitude dominates the others and becomes the DL. It then starts to hinder hot electron free-streaming and produces an obvious drop in T_e as can be
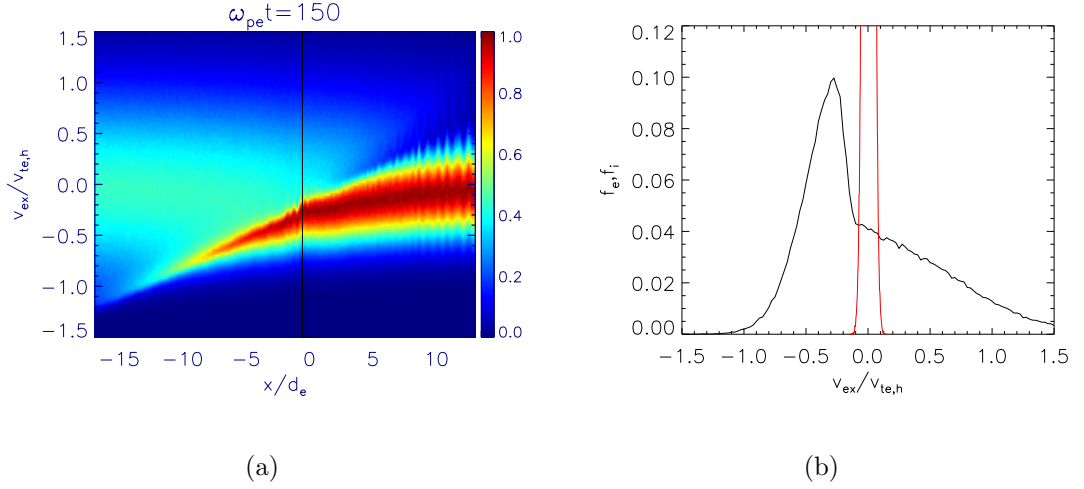
Figure 3.6: (a) Electron phase space at $\omega_{pe}t$=150 and (b) a cut of (a) at the position of the DL at x$\sim$ -1d_e, indicated by a vertical black line. The ion distribution f_i (red) is overlaid on the electron distribution f_e (black). Since the ions and cold electrons have the same temperatures, the ion thermal speed is $\sim \sqrt{m_i/m_e}$=10 times lower than the return current thermal speed. The integrated areas under the curves (i.e., their densities) are the same, so f_i peaks at $\sim$10 times the height of f_e. The vertical scale is normalized to the maximum of f_i.

seen at $\omega_{pe}t$=150. The two smaller peaks on either side of x=0 later turn into fairly symmetric waves, which produce no significant potential jump. The wave turbulence from which the DL emerges is driven by the return current interacting with the background ions. The DL is also driven by this streaming instability, whose origin is now described.

3.4   DL Generation Mechanism: Streaming Instability

Figure 3.6(a) shows the electron phase space at $\omega_{pe}t$=150. The hot and cold electron distributions are at the left and right sides, respectively. Note the narrower thermal spread of the cold electrons at the right, as well as the wider spread of hot electrons at the left. The initial temperature transition is near x=0. A beam

of cold electrons is entering the hot region. At $\omega_{pe}t=0$, both distributions are non-drifting and there is no beam. As the hot electrons free-stream into the cold electron region, ions cannot follow and are left behind as a charge imbalance. The resulting electric field drags a cold electron beam towards the hot electron region as a return current. The relative drift between this return current and the ions excites the instability. Fig. 3.6(b) is a cut of the phase space at the position of the DL ($x\sim$ -1d_e). The return current, with a negative beam speed, sits on top of the streaming hot distribution, which is moving to the right and has a wider thermal spread. The drift of the return current electrons with respect to the ions (red) excites the ion/return-current-electron streaming instability. The linear growth rate γ of the ion-electron streaming instability (also known as the Buneman instability (Buneman (1958))) for the most unstable wave calculated in (two-)fluid theory[2] is given by

$$\gamma = \frac{\sqrt{3}}{2}\left(\frac{m_e}{2m_i}\right)^{1/3}\omega_{pe}. \tag{3.1}$$

Using the parameters of our simulation, $\gamma \sim 0.15\,\omega_{pe}$. The growth time τ is thus $\tau \sim \gamma^{-1} \sim 7\,\omega_{pe}^{-1}$. The instability is sufficiently strong to produce the DL at $\omega_{pe}t\sim 100$. We also note that the background magnetic field is not significantly perturbed.

The time evolution of the electron phase space reveals that the growth of the DL depends on the number of return current (RC) electrons reflected at the foot of

[2]In a two-fluid model of plasma, ions are considered as a fluid and hence, all ions move at the same speed, so are electrons. It is helpful to compare fluid theory with kinetic theory that allows for different velocities in a particle distribution. The Buneman instability is a fluid-like instabilty because the drift of the electrons relative to the ions is greater than the electron thermal speed. Therefore, the ions see all the electrons moving at one single speed.
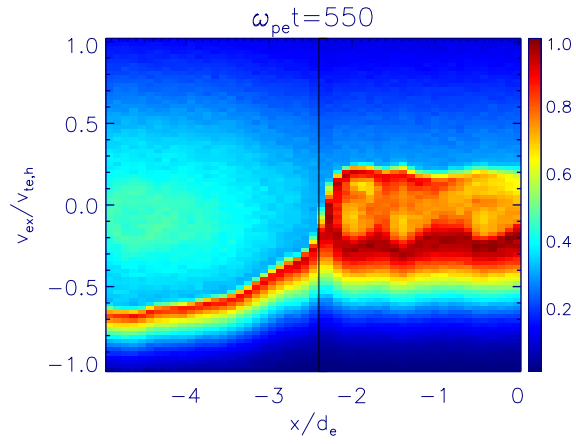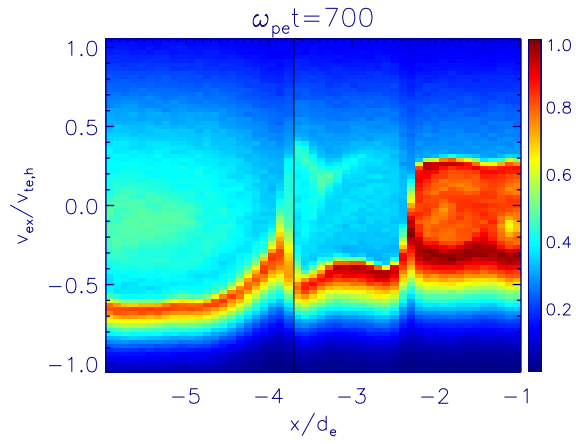
Figure 3.7: Electron phase spaces at: (a) $\omega_{pe}t$=550; and (b) $\omega_{pe}t$=700. The vertical black lines mark the low potential side of the DL and to its right is the negative leg E_x of the DL that can reflect the return current electron beam.

the DL. One can see from Fig. 3.4 that the electric field E_x of the DL has a negative

leg on the low T_e side. This shows up as a potential dip on the low potential

side. The RC electrons are reflected by the negative leg, which effectively reduces

the RC speed and thus converts the kinetic energy of the RC to the electrostatic

energy of the DL. By exchanging momentum with the reflected electrons, the DL

gets amplified Lotko (1983). Electron reflection also indicates when the instability

enters into a nonlinear regime (ω_{pe}t>150). The DL growth depends on the number

of RC electrons reflected at the foot of the DL. Qualitatively, the dependence of DL

growth on the number of reflected electrons can be seen by contrasting the phase

space at a time when the DL is growing, e.g., at ω_{pe}t=550, with a time when it is

not growing, e.g., at ω_{pe}t=700 (as $e\phi_{DL}/T_{e,h}$ plateaus in Fig. 3.3(b)). At ω_{pe}t=700

(Fig. 3.7(b)) to the right of the DL at x -4d_e (vertical black line), there are many

fewer reflected electrons than to the right of the DL at ω_{pe}t=550 (Fig. 3.7(a)),

x -2d_e. We estimated the number of reflected RC electrons, N_{ref}, by integrating

the electron distribution to the right of the DL over a distance of one d_e, which

is the typical width of the DL, and for $v_{ex} \in$(0, 0.4 $v_{te,h}$), which is approximately

the velocity range covered by the reflected RC electrons as they turn around and

acquire positive velocities. N_{ref} is normalized to N_0, the initial electron number

contained in the same interval. Note that the integration for N_{ref} also includes a

contribution from hot free-streaming population in that velocity range. However,

this contribution stays nearly constant and the variation in N_{ref} mainly comes from

the change in the number of reflected cold RC electrons. Therefore, N_{ref} suffices

as an estimate of the reflected RC electrons (plus some constant offset). N_{ref}/N_0

(green) is plotted on top of the DL strength, $e\phi_{DL}/T_{e,h}$, in Fig. 3.3(b) to show their correlation. As N_{ref}/N_0 increases during $\omega_{pe}t\leq550$ and ≥950, $e\phi_{DL}/T_{e,h}$ has a general increasing tendency as well. As N_{ref} drops abruptly at $\omega_{pe}t=550$ and stays at a low level until $\omega_{pe}t=950$, $e\phi_{DL}/T_{e,h}$ plateaus. Hence, there is good correlation between the DL growth and the number of the reflected RC electrons.

An examination of the evolution of the electric field in Fig. 3.3(a) reveals that at $\omega_{pe}t\sim550$, the DL sheds an ion-acoustic shock wave, which shows up as an ion hole in ion phase space. Once it leaves the DL, the shock accelerates to the right while the DL continues to slowly move to the left. Therefore, their separation increases. The shock wave is bipolar and reflects most of the RC electrons with its large-amplitude negative leg. One can see in Fig. 3.7(b), at $\omega_{pe}t=700$, most of the RC electrons are reflected behind the shock at x -$2d_e$. N_{ref}/N_0 shows an abrupt drop at $\omega_{pe}t=550$ because most of the RC electrons are stuck behind the shock and do not reach the DL. The shock dissipates through ion heating. The ion temperature increases by as much as a factor of two along the path traversed by the shock. The shock gradually diminishes in amplitude. Similar dynamics (acceleration and decay) of an ion hole mode at the low potential side of a weak DL created in ion-acoustic turbulence is also observed in current-driven systems Barnes et al. (1985).

During our simulation, $e\phi_{DL}/T_{e,h}$ reaches 0.8 at $\omega_{pe}t=1200$ (Fig. 3.4). This means that hot electrons with velocities $v/v_{te,h} \leq \sqrt{0.8} \sim 0.9$ will be reflected. The electron phase space at $\omega_{pe}t=1200$ in Fig. 3.8 shows that the population of hot electrons with $v/v_{te,h} \leq 0.9$ wraps around from positive to negative velocities when
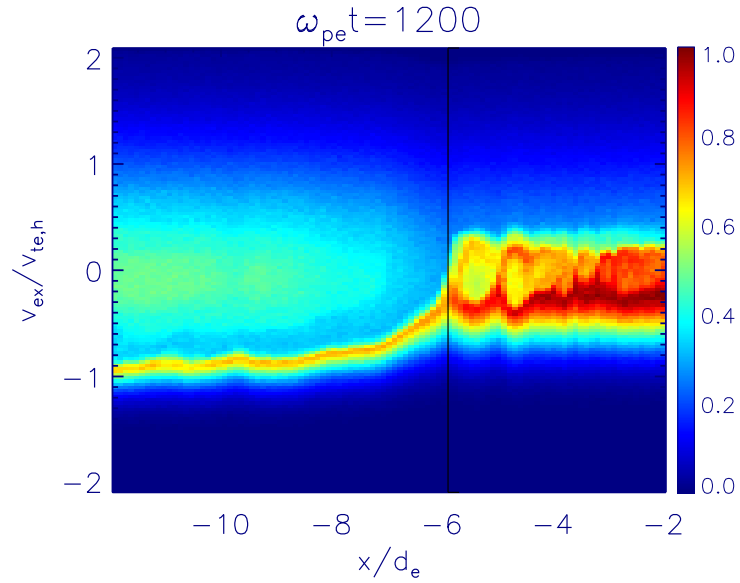
Figure 3.8: Electron phase space at $\omega_{pe}t=1200$ with $e\phi_{DL}/T_{e,h} \sim 0.8$. To the left of the DL location, x$\sim$ -6d_e, hot electron populations with $v/v_{te,h} < 0.9$ (cyan and green in color) are reflected by the potential barrier. They are trapped in the hot region. For higher velocity electrons (at the tail; blue in color), there is a drop in velocity as they are decelerated. Both contribute to suppression of the heat flux.

encountering the DL. They are reflected and hence confined in the source region. The suppression observed here is significant. We calculate the heat flux carried by kinetic hot electrons that is positively directed as $Q(x,t){=}\frac{1}{2}m_e \int\limits_0^\infty v^3 f_e(x,v,t)dv$ (Krall and Trivelpiece, 1973). The mean flow speed is <2% of the hot electron thermal speed and hence negligible in the calculation of $Q(x,t)$. Similar to T_e, Q has a sharp jump across the DL. Towards the end of the simulation, Q is suppressed by $\sim$40% to the right of the DL compared with the higher value to the left of the DL.

3.5 Discussion on the DL model

The DL suppression mechanism, by reflection, differs from the conventional picture of electron scattering by ion-acoustic turbulence (Manheimer, 1977), which was studied in unmagnetized (laser fusion) plasmas. Multi-dimensional computer simulations show that current-driven ion-acoustic turbulent spectrum is flared out within about 45° of the current direction (Biskamp and Chodura, 1971; Biskamp et al., 1972; Dum et al., 1974). The presence of a background magnetic field, as in solar flare systems, will likely inhibit scattering perpendicular to the field, making it less effective in suppressing the transport of hot electrons. The inhibition of perpendicular scattering is observed in systems in which two fast electron beams interact and electromagnetic turbulence arises from electron streaming instabilities, but perpendicular deflection by magnetic field turbulence is suppressed by the tension force of the background field (Lee and Büchner, 2011). The DL suppression mechanism, which does not involve perpendicular deflection, is, however, not weakened by the presence of a background magnetic field.

3.6 Application to Looptop X-ray sources

In the above-the-looptop HXR sources, Krucker et al. (2010, 2007) showed an exponential decay of the HXR time profiles on a timescale of more than two orders of magnitude longer than the electron transit time through the source. The formation of a DL provides a plausible mechanism to confine energetic electrons in the source

region. Electrons that have kinetic energies less than the potential drop of the DL are reflected back to the source region. Over the entire course of the simulations, the DL tends to amplify through multiple phases of growth. There are no signs of decay. Since it is driven by the return current electrons, which exist for as long as some hot electrons are leaking out, the DL can persist until the eventual depletion of all hot electrons in the source region, which should take much longer than the electron transit time through the source due to the strong transport suppression caused by the DL. The DL lifetime is therefore expected to be much longer than the transit time. This can naturally explain the prolonged lifetimes (>100 s) of the energetic electrons from the above-the-looptop HXR observations compared with the electron transit time (∼1 s) through the source.

3.7   Conclusion on Transport Suppression by DLs

During flares and coronal mass ejections, energetic electrons from coronal sources typically have very long lifetimes compared to the transit times across the systems, suggesting confinement in the source region. Particle-in-cell simulations are carried out to explore the mechanisms of energetic electron transport from the corona to the chromosphere and possible confinement. We set up an initial system of pre-accelerated hot electrons in contact with ambient cold electrons along the local magnetic field, and let it evolve over time. Suppression of transport by a non-linear, highly localized electrostatic electric field (in the form of a double layer) is observed after a short phase of free-streaming by hot electrons. The double layer

(DL) emerges at the contact of the two electron populations. It is driven by an ion-electron streaming instability due to the drift of the back-streaming return current electrons interacting with the ions. The DL grows over time and supports a significant drop in temperature and hence reduces heat flux between the two regions that is sustained for the duration of the simulation. This study shows transport suppression begins when the energetic electrons start to propagate away from a coronal acceleration site. It also implies confinement of energetic electrons with kinetic energies less than the electrostatic energy of the DL for the DL lifetime, which is much longer than the electron transit time through the source region.

Chapter 4

Saturation Mechanism of DLs

The degree of transport suppression depends on the maximum strength of the DL at saturation. In Chapter 3, the generation mechanism of a DL was studied and identified as the Buneman instability involving the ions and return current electrons. In this chapter, we investigate the saturation mechanism of the DL with simulations and analytic modeling. We carry out a series of simulations with different initial values of the hot electron temperature and show that the DL potential at saturation scales linearly with the hot electron temperature. The DL saturates when its potential jump is large enough to accelerate ions above the local sound speed. The result is a parallel ion acoustic shock that stabilizes the Buneman instability and therefore saturates the DL. We demonstrate that the shock formation criterion predicts a maximum DL strength that is proportional to the hot electron temperature in agreement with simulations. At its maximum strength, the DL is observed to reflect, and hence contain, a significant fraction of electrons in the source.

An outline of this chapter is as follows: the setup of the simulations and parameters used for flare settings are described in Section 4.1; in Sections 4.2 and 4.3, results from the simulations and the shock model are presented and we provide evidence for the model and determine the saturation amplitude of a DL; and we summarize in Section 4.4.

4.1 Simulation setup for scaling DL Strength

The initial setup here is the same as in Section 3.1. We perform three simulations with increasing $T_{h0,\parallel}$=0.5, 1 and 2 (the first one has been extensively discussed in Chapter 3). All hot electrons have unity plasma beta β in the parallel direction. β_{h0} is maintained at the same value for different T_{h0} by varying B_0, which is not expected to affect the results since the phenomenon observed here is dominantly electrostatic. The magnetic field is not significantly perturbed in the simulations. Outside of the hot electron region, the ambient (cold) electron temperature T_{c0} is 0.1 for all runs. The ratios of hot to cold (parallel) electron temperatures are, therefore, $T_{h0/T_{c0}}$= 5, 10 and 20, respectively, for the three runs. This increasing contrast in temperature allows us to study how the strength of a DL scales to the real system that has over three orders of magnitude in separation of scales.

Different T_{h0} corresponds to a different value of the Debye length λ_{De}, so it is more suitable to normalize space with λ_{De} from here on to reflect the change (although d_e is used in Chapter 3). In λ_{De}, the size of the simulations is $L_x \times L_y$= 6553.6 $\times$ 25.6 λ_{De}^2 with a grid size of 0.2$\times$0.2 λ_{De}^2 for T_{h0}=0.5. For T_{h0}=2, λ_{De} is twice as big, so the grid size is 0.1 λ_{De}. In all cases, λ_{De} is well resolved. The domain size is the same when measured in terms of electron inertial lengths d_e=c/ω_{pe} for all three T_{h0}. Hence, higher T_{h0} runs with hotter electrons are evolved for shorter periods of time than the lowest T_{h0} run.
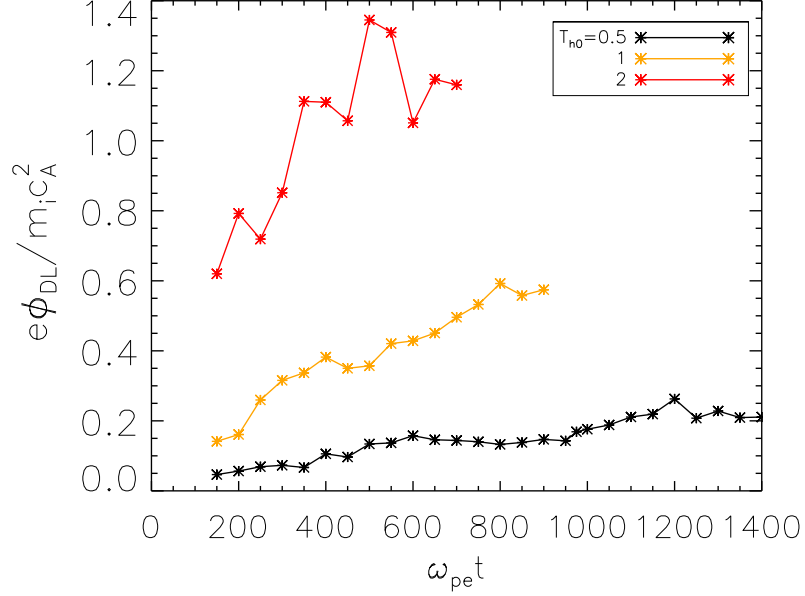
Figure 4.1: Evolution of the DL strength $e\phi_{DL}$ in simulations of different T_{h0}.

4.2 Scaling Result in Simulations

Figure 4.1 shows the time evolution of the DL strength in three simulations with increasing initial hot electron temperatures T_{h0}=0.5, 1 and 2. A similar cycle of DL growth followed by saturation is observed. As the contrast between hot and cold temperatures increases, the instability becomes stronger and develops more rapidly, leading to faster and further strengthening of the DL. For the same system size, i.e., for about the same distance traveled by the hot electrons, the maximum strength $e\phi_{DL}^{max}$ the DL reaches is higher in higher temperature runs. $e\phi_{DL}^{max}$ is plotted in Figure 4.2. A good linear fit (dashed line) of $e\phi_{DL}^{max} = 0.73T_{h0} - 0.11$ with a coefficient of determination of 0.9998 is obtained. It indicates that the maximum strength of the DL scales linearly with the initial hot electron temperature. It also implies a threshold on the lowest possible T_{h0} for DL formation. However, this threshold is
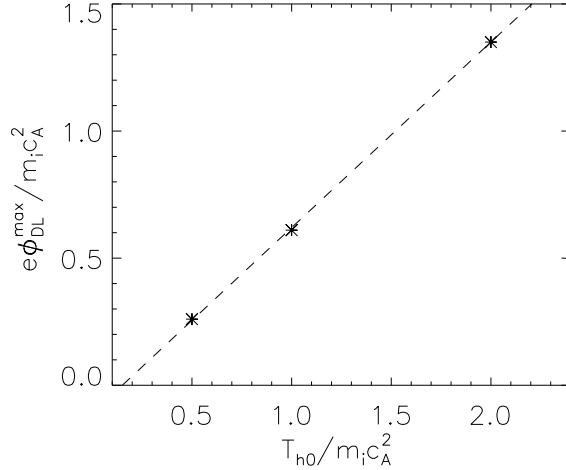
Figure 4.2: Maximum DL strength $e\phi_{DL}^{max}$ from simulations of increasing T_{h0}.

not considered reliable as the regime of very low T_{h0} is not explored and the behavior is not known. We therefore take the fit to be approximately $\tilde{\phi}^{max} \equiv e\phi_{DL}^{max}/T_{h0} \sim$ 0.73.

4.3   Shock Model

The physics occurring at the contact between the hot and cold electrons plays a crucial role in whether the hot electrons propagate out or are confined within the region. Initially, the hot electrons propagate by free-streaming along the magnetic field. Ions, being less mobile, lag behind. This creates a charge imbalance in the hot region, which draws in an electron beam from the cold electrons as a return current (RC). The RC electrons drift relative to the ions, exciting an ion-electron streaming instability, identified as the Buneman instability (Chapter 3). It is the driver of the DL. As the DL forms at the contact between the two populations, hot electrons with kinetic energy less than the DL potential $e\phi_{DL}$ are reflected. The stronger the DL,
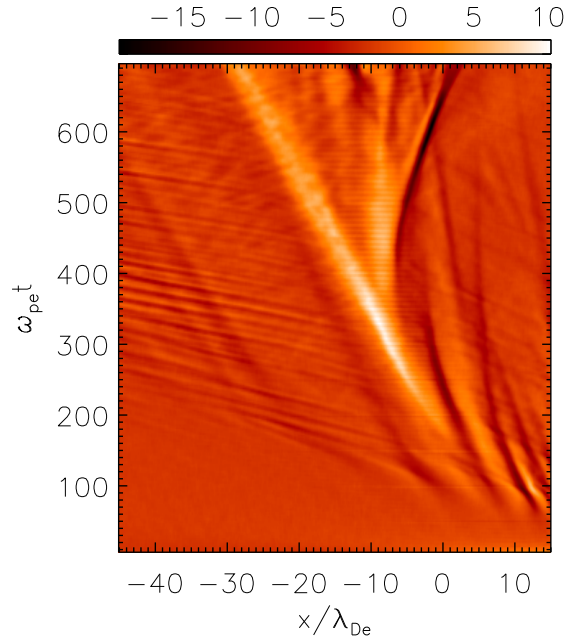
Figure 4.3: Time evolution of the electric field E_x from the highest temperature (T_{h0}=2) run.

the more reflected electrons and hence the fewer escaping hot electrons.

The maximum strength of a DL depends on its saturation mechanism. We observe that saturation is linked to the formation of a shock in our simulations. In the following, we show data from the highest temperature run to demonstrate this. Figure 4.3 shows the time evolution of the electric field E_x from that run. Data are averaged in y. The bright white feature around ω_{pe}t=250-350 is the DL. It drifts to the left over time. A rightward propagating shock forms and starts to part from the DL at ω_{pe}t 350, forming an intense negative electric field later in time. Around ω_{pe}t $\sim$ 350 is when the DL starts to saturate (red curve plateauing in Figure 4.1). It is observed from all the simulations that whenever a shock forms, the DL stops strengthening (see, also, data from the lowest T_{h0} run in Figure 3.3 from Chapter 3).
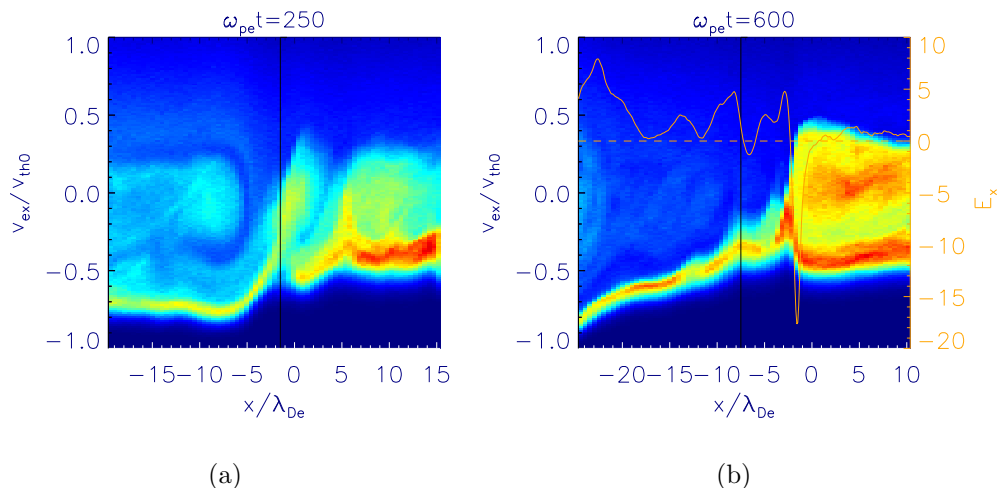
Figure 4.4: Electron phase space, in a simulation with $T_{h0} = 2$, at a time during the DL growth at $\omega_{pe}t=250$ (a) and during saturation at $\omega_{pe}t=600$ (b). The same color scale is used for both. Velocities are normalized to the initial hot electron thermal speed v_{th0}. E_x (orange) is overlaid on (b) to show the position of a shock that has a strong negative electric field.

The shock is driven by ions accelerated to high velocities in the positive x direction, which will be further discussed later, so it propagates to the right and decouples from the DL.

4.3.1 Shock Stabilizing the Instability

Shock formation saturates the DL growth by stabilizing the Buneman instability. In Figure 4.1, for example, the evolution of the DL strength $e\phi_{DL}$ from the highest T_{h0} run (red) indicates a growth phase before $\omega_{pe}t=350$ and in general a saturation phase after that. DL saturation is also evident from the decrease in E_x of the DL after $\omega_{pe}t=350$ in Figure 4.3. In the following, we explain how the shock stabilizes the instability by reducing the speed of the RC beam that is the driver

of the instability. Evidence is observed in the electron phase space. We show in Figure 4.4 the electron phase space at a time during the growth phase, at ω_{pe}t=250 (a), and during the saturation phase, at ω_{pe}t=600 (b). E_x (orange) is overlaid in (b) to show the location of the shock that has a large-amplitude negative peak in E_x. A vertical black line denotes the low potential side of the DL. To its left is the hot electron population (note the reflected hot electrons (cyan) in (a) with their velocities wrapping from positive to negative). To the right of the vertical black line is the RC beam. The speed of the RC beam at the DL during the saturation phase in (b) is $|v_d| < 0.5v_{th0}$, which is noticeably lower than that during the growth phase, which is $|v_d| > 0.5v_{th0}$ in (a). At ω_{pe}t=600, the shock is at $x \sim -2\lambda_{De}$. Its large-amplitude negative leg significantly reduces the speed of the RC beam that is drifting in the negative x direction, and even reflects a significant number of RC electrons, i.e., from negative to positive velocities. The surviving beam that reaches the DL (vertical black line) has a much lower speed and is stable to the Buneman instability. Note that the reflection of the RC electrons at the DL due to trapping by the Buneman instability, which drives up the DL amplitude (see Chapter 3), is absent at ω_{pe}t=600.
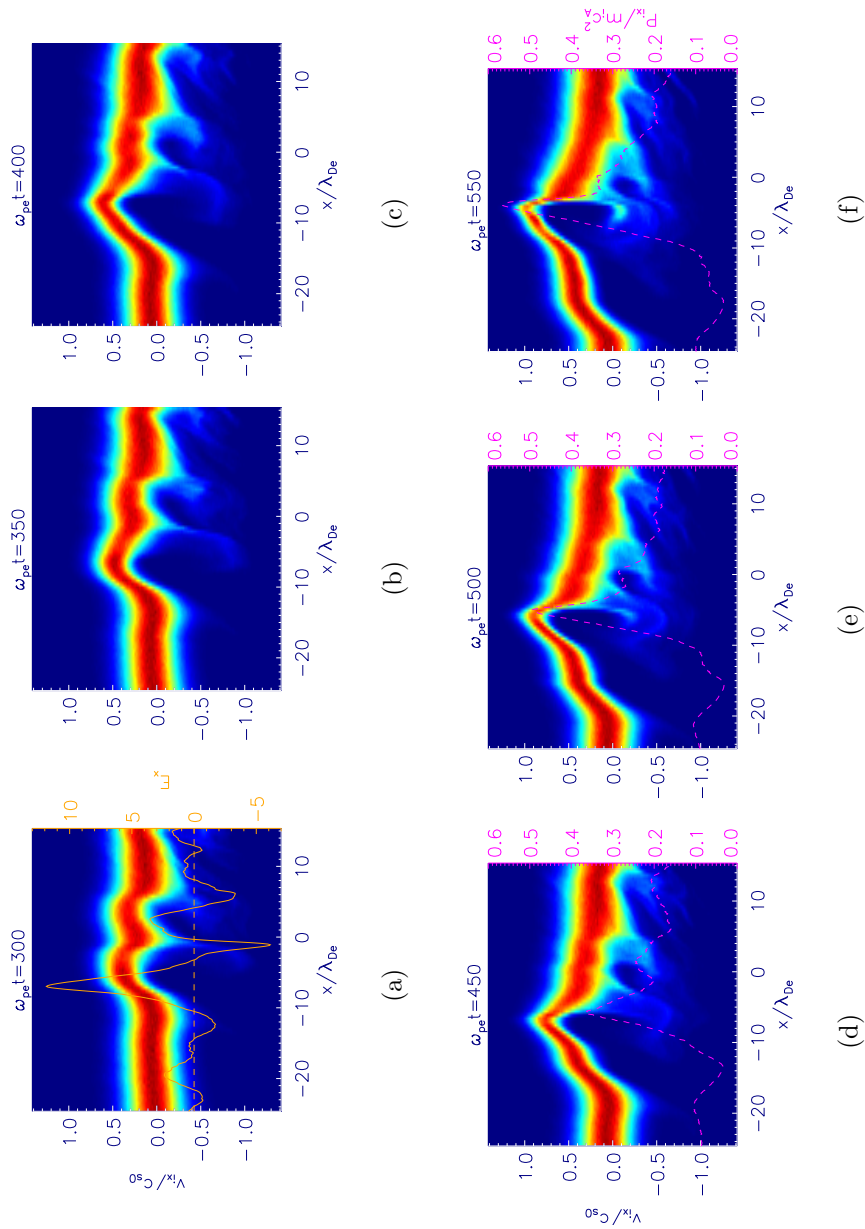
Figure 4.5: Ion phase space before and during the formation of the shock from the highest T_{h0} run. Velocities are normalized to ion sound speed c_{s0} based on the initial hot electron temperature. The same color scale is used for all. Overlaid in (a) is the electric field E_x (orange), and in (d)-(f) is the parallel ion pressure P_{ix} (magenta).

4.3.2   Driver of the Shock and Maximum DL Strength

It is observed from the ion phase space that the shock is driven by ion acceleration to high velocities, beyond the ion sound speed, at the DL. Figure 4.5 shows the evolution of the ion phase space before and during the formation of the shock. The electric field E_x (orange) is overlaid in (a) to show the position of the DL, and the parallel ion pressure P_{ix} (magenta) in (d)-(f) to show the steepening of the shock. Velocities are normalized to the sound speed $c_{s0} \approx \sqrt{T_{h0}/m_i}$ based on the initial hot electron temperature (recall that the simulations and the coronal energetic electron sources are in the limit where the electron temperature is much greater than the ion temperature). In (a), at ω_{pe}t=300, ions are strongly accelerated at the location of the DL, which is the large positive peak in E_x. Over time, they are further accelerated and around ω_{pe}t=400 (c), some ions reach c_{s0} and to their right, a jump in their velocity is developing. From ω_{pe}t=450 (d) and later, ion velocities at the DL surpass c_{s0} with a velocity jump forming at the right of the "supersonic" ions. Velocities drop from supersonic to subsonic over a narrow transition less than the DL width (which is $\sim 10\lambda_{De}$). P_{ix} also abruptly increases across the shock as expected. Thermalization of the ions is likely due to trapping in the large amplitude waves within the transition (Figure 4.5) as studied previously (Quest, 1988). These observations lead us to conclude that the shock is driven by ion acceleration at the DL. The stronger the DL, the higher the ion velocity. Figure 4.6 shows the evolution of the maximum ion velocity measured from the ion phase space (solid), and ion velocity based on acceleration by the DL potential, $v_{i,DL} = \sqrt{2e\phi_{DL}/m_i}$ (dashed).

$v_{i,DL}$ resembles the shape of the red curve in Figure 4.1 since it is based on the DL potential. The solid and dashed curves are consistent with each other, and hence indicate that the accelerated ions are produced by the DL potential.
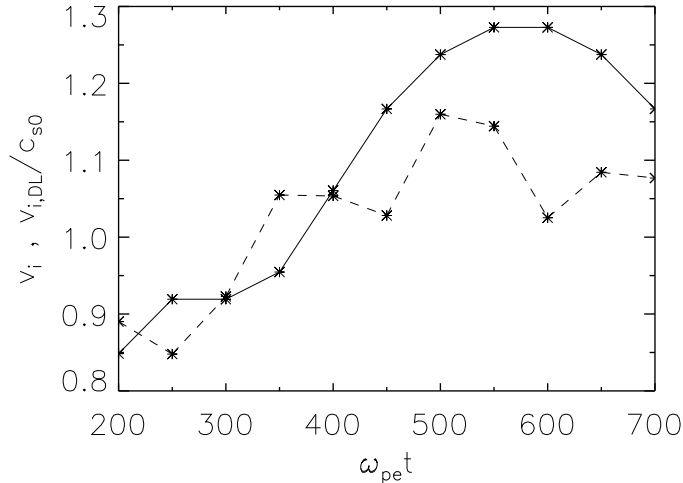
Figure 4.6: Time evolution of the measured maximum ion velocity from the ion phase space, v_i (solid) and ion velocity based on acceleration by the DL, $v_{i,DL}$ (dashed).

We note that by the time the DL saturates in the simulation, the local electron temperature T_h at the DL drops to $\sim 0.75 T_{h0}$ (because a fraction of hot electrons escape from the source region), so the local sound speed $c_s (\approx \sqrt{T_h/m_i})$ is lower than c_{s0}. That is probably why the shock is generated even though the accelerated ion velocities only marginally exceed c_{s0} in Figure 4.5(c).

Since the DL accelerates ions, which eventually drives a shock that in turn stabilizes the instability and saturates the DL growth, we can use the shock formation criterion, namely, ion acceleration to supersonic speed, to determine the maximum

strength of the DL.

$$v_i \sim \sqrt{\frac{2e\phi_{DL}}{m_i}} > c_s \sim \sqrt{\frac{T_h}{m_i}}$$

$$\frac{e\phi_{DL}}{T_h} > \frac{1}{2} \tag{4.1}$$

Normalizing to T_{h0} for comparison with simulations, we have:

$$\frac{e\phi_{DL}}{T_{h0}} > \frac{1}{2}\frac{T_h}{T_{h0}} \tag{4.2}$$

Approximating $T_h \sim 0.75 T_{h0}$, Equation 4.2 gives $e\phi_{DL}/T_{h0}$ 0.4. As soon as the DL reaches a strength of 0.4 T_{h0}, a shock forms, leading to DL saturation. This equation shows that the saturated DL strength scales linearly with the hot electron temperature, which is consistent with the result in Figure 4.2. The maximum DL strength based on this shock model is $\tilde{\phi}^{max} = e\phi_{DL}^{max}/T_{h0} \sim 0.4$. This value agrees with the measurement from our simulations within a factor of two.

We note that this prediction is independent of the ion-to-electron mass ratio. It is therefore applicable to realistic systems with real mass ratio.

4.3.3 Escaping Electron Density n_{esp}

To quantify the degree of confinement, we can compare the ratio of either the reflected electron density in the hot source or the escaping electron density to the total density. In the following, we calculate the escaping hot electron density n_{esp} after passing through a potential barrier $e\phi_{DL}$. Given the initial hot electron distribution function f_{e0}, which is a Maxwellian distribution, and $e\phi_{DL}$, n_{esp} can be expressed analytically by integrating f_{e0} over velocities of the escaping electrons. f_{e0} is a function of both parallel and perpendicular velocities, so a 3D volume integral

$\int d^3v$ needs to be performed. However, the DL is a parallel electric field and only reduces electron velocities in the parallel direction. The integral $\int f_{e0} d^3v$ is therefore separable in $v_\parallel$ and $v_\perp$. The perpendicular contribution gives unity, so n_{esp} is reduced to a 1D integral over only the parallel velocities. For simplicity, we drop "$\parallel$" in "$v_\parallel$" in the calculation below. Note that it suffices to consider either side of the contact since the system under consideration is symmetric. We choose the right side where the escaping hot electrons move to the right and thus have positive velocities. We then have:

$$\begin{aligned} n_{esp} &= \int_b^\infty f_{e0} \, dv \qquad ; b \equiv \sqrt{\frac{2e\phi_{DL}}{m_e}} \\ &= \frac{n_0}{\sqrt{\pi}\, v_{th0}} \int_b^\infty e^{-v^2/v_{th0}^2} \, dv \\ &= \frac{n_0}{2} \operatorname{erfc}(\tilde{\phi}^{1/2}) \qquad ; \tilde{\phi}^{1/2} = \frac{b}{v_{th0}} \end{aligned} \qquad (4.3)$$

where $\operatorname{erfc}(z) = \frac{2}{\sqrt{\pi}} \int_z^\infty e^{-t^2} \, dt$ is the complementary error function. The total density of hot electrons moving to the right is $n_{tot} = \int_0^\infty f_{e0} \, dv = n_0/2$, so the ratio of escaping to total density is

$$\tilde{n}_{esp} \equiv \frac{n_{esp}}{n_{tot}} = \operatorname{erfc}(\tilde{\phi}^{1/2}) \qquad (4.4)$$

As $\tilde{\phi}$ increases, $\tilde{n}_{esp}$ decreases, i.e., fewer hot electrons escape. This tendency is also observed in the simulations. For example, at lower values of $\tilde{\phi}$ before the DL saturates, $\tilde{n}_{esp}$ is measured to be higher than the value at saturation. Using $\tilde{\phi} \sim 0.7$ obtained in Section 4.2, Equation 4.4 yields $\tilde{n}_{esp} \sim 0.24$. In the simulations, $\tilde{n}_{esp} \sim 0.25 n_0/n_{tot} = 0.5$, which is within a factor of two from the prediction. This value of escaping density implies that about 50% of the total density is trapped in the source region. Thus, a substantial number of electrons are confined.

4.4 Conclusion on DL saturation mechanism

From recent PIC simulations of a pre-accelerated hot electron source, chosen as a basic model of flare-heated coronal sources, it is observed that the transport of the hot electrons is significantly suppressed by the formation of a DL (Chapter 3). The degree of suppression depends on the strength of the DL. In this work, a series of PIC simulations are performed to obtain a scaling of the DL strength with the hot electron temperature. A linear scaling relation is observed. The amplitude of the DL is limited by the formation of sound wave shocks produced by ions accelerated through the DL potential. An analytic calculation based on this model yields a linear scaling with the hot electron temperature, a result consistent with simulations. This study shows that a substantial fraction of electrons is confined by the DL. Thus, DLs can produce the electron confinement suggested by obervations of X-ray emission in the solar corona.

Chapter 5

Confinement by a DL and Magnetic Mirror

We observe that an anisotropy develops in the hot electrons that pass through a DL. This is because the parallel velocities are reduced by the DL while the perpendicular velocities are not affected. This causes an anisotropy with $T_\perp > T_\parallel$ downstream from the DL. We indeed observe a pancake distribution, as discussed in the next section. An anisotropic (pancake) distribution favors further hot electron trapping in the presence of a magnetic mirror. Since the magnetic geometry of flaring loops resembles a mirror configuration, we explore combining a magnetic mirror with the DL. We demonstrate that the combination significantly enhances confinement.

5.1 Velocity-space Anisotropy due to the DL

It is easier to identify an anisotropy due to the DL when starting with an isotropic distribution, so a simulation with the same parameters as the highest temperature run ($T_{h0,\parallel}$=2) described in Section 4.1, except for using an isotropic distribution for the hot electrons, i.e., $T_{h0,\perp}=T_{h0,\parallel}$, L_x being half of the original and L_y being twice the original, is performed. Figure 5.1 shows the electron distributions versus velocities parallel (v_{ex}) and perpendicular (v_{ey}) to the background magnetic
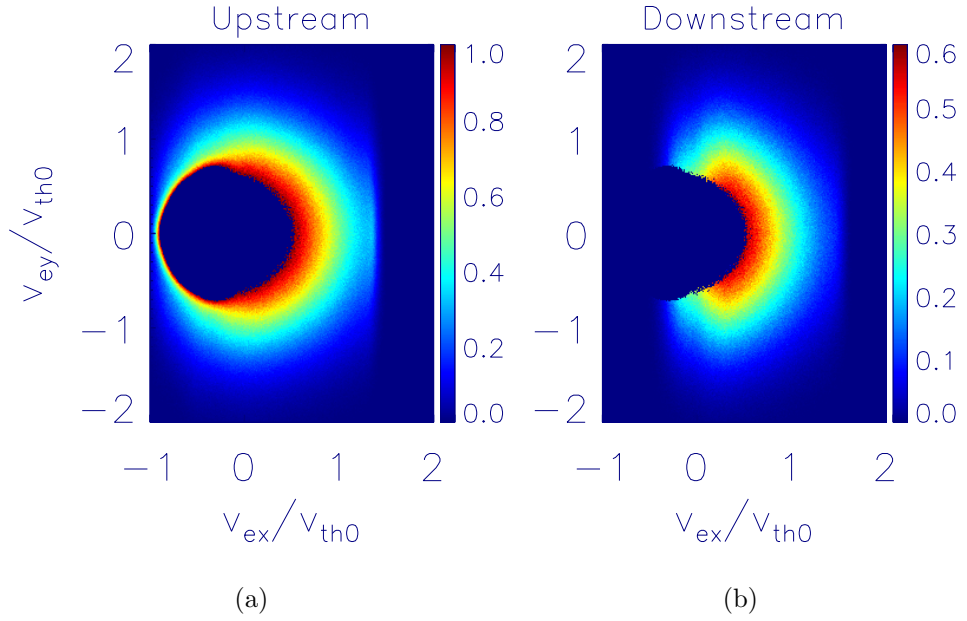
Figure 5.1: Electron distribution (a) before and (b) after passing through a DL. Anisotropy develops in the escaping hot electrons downstream from the DL. Values are normalized to the maximum in (a). Note (b) has a different color scale than (a).

field, near the end of the run, at $\omega_{pe}t$=350. They are from locations (a) upstream, i.e., before the hot electrons encounter the DL, and (b) downstream, i.e, after some of them escape from the DL. They are sampled over a space of 50 λ_{De} in x, several times the width of the DL. A lower-velocity region is masked since it contains the cold RC electron beam, which has a much higher peak phase space density than the hot electrons and will therefore overshadow the latter. In (a), the distribution takes on a circular shape. Hot electrons are nearly isotropic upstream. After passing through the potential barrier of the DL, the parallel velocity is reduced while the perpendicular velocity is unchanged. This gives rise to an anisotropy downstream from the DL in (b). The parallel temperature is now lower than the perpendicular value, which results in a pancake distribution. A cutoff at higher v_{ex} develops as
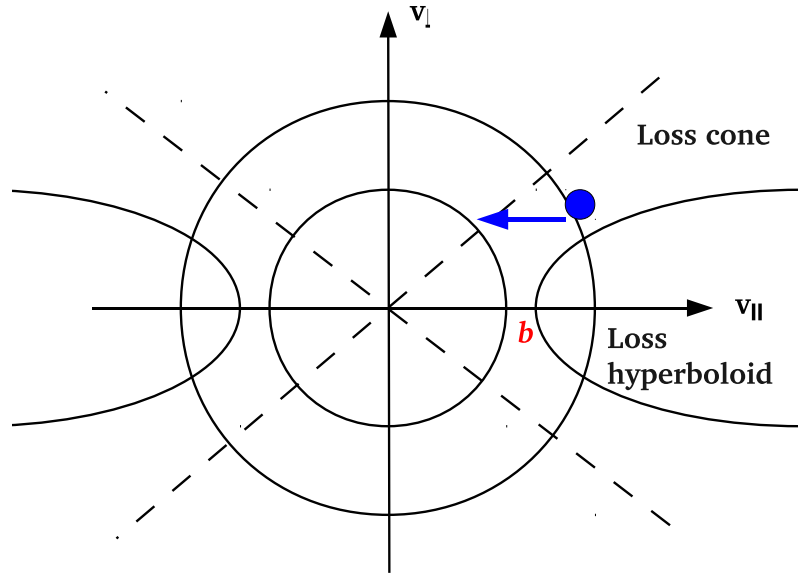
Figure 5.2: Schematic of a loss cone in a 2D distribution function at the presence of a magnetic mirror. A loss cone becomes a loss hyperboloid when a potential is also present.

high velocity electrons leave the regions upstream and downstream of the DL by the end of the simulation.

Since a pancake distribution is preferentially trapped in a magnetic mirror and the geometry of a flare loop resembles a magnetic mirror, we next explore combining the DL with a mirror for the possibility of enhanced confinement.

5.2   Combining with a Magnetic Mirror

In the presence of a magnetic mirror, particles outside of a loss cone will be trapped. For the 2D velocity space sketched in Figure 5.2, the loss cone is bounded by the 2 dashed lines. When including a potential (provided by a DL here) as well,

the loss cone becomes a hyperboloid defined by the following equation:

$$v_\parallel^2 - v_\perp^2(r-1) = \frac{2e\phi_{DL}}{m_e} \tag{5.1}$$

where r is the mirror ratio and ϕ_{DL} is the DL potential. See Appendix A for a derivation. In the limit $\phi_{DL} \to 0$, this reduces to a cone. Also shown in Figure 5.2 are two contours of constant total energy. When going through a DL, an electron labeled as a blue blob will move to lower parallel velocity while its perpendicular velocity remains unchanged (following the blue arrow). This will create an anisotropy, helping to move electrons out of the loss cone.

The hyperboloid intersects with the $v_\parallel$ axis at a value $b = \sqrt{2e\phi_{DL}/m_e}$ (labeled in red). For a stronger DL, i.e., larger ϕ_{DL}, b has a greater value. This moves the loss hyperboloid to the right, resulting in a reduced overlap with the electron distribution. Therefore, fewer electrons will be lost. The same is true for a larger mirror ratio for which the hyperboloid closes closer to the $v_\parallel$ axis, making it thinner and hence the phase volume smaller.

.

5.3   Escaping Electron Density with the Addition of a Mirror

We now quantify the degree of electron confinement in the combined system. A similar calculation to that in Section 4.3.3 is carried out to determine the escaping electron density. We integrate the initial distribution over the loss hyperboloid. A derivation is given in Appendix B. The escaping density normalized to total density
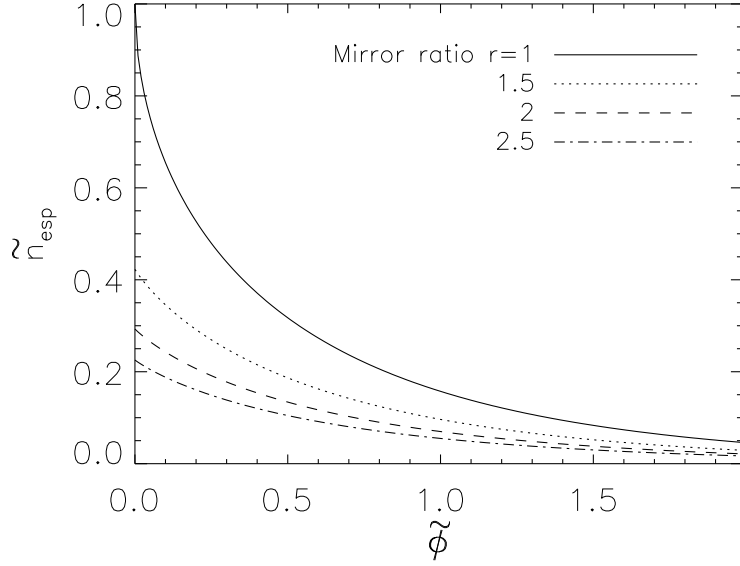
Figure 5.3: $\tilde{n}_{esp}$ as a function of $\tilde{\phi}$ for several mirror ratios r, for an isotropic distribution.

is given by:

$$\tilde{n}_{esp} = \mathrm{erfc}(\tilde{\phi}^{1/2}) - \exp[\tilde{\phi}/A(r-1)]\,\mathrm{erfc}([\tilde{\phi}X]^{1/2})/X^{1/2}$$

$$; A \equiv \frac{T_\perp}{T_\parallel},\ X \equiv 1 + \frac{1}{A(r-1)}$$

(5.2)

$\tilde{n}_{esp}$ is plotted for several mirror ratios r in Figure 5.3, assuming isotropic initial electron distributions (A=1). The r=1 case, corresponding to the presence of a DL alone, is taken from Equation 4.4 and plotted for comparison with cases with a mirror. With neither a DL nor a mirror, i.e., for $\tilde{\phi}$=0 and r=1, all electrons escape, so $\tilde{n}_{esp}$=1. $\tilde{n}_{esp}$ decreases with increasing $\tilde{\phi}$ and r. A typical mirror ratio of 2 to 2.5 from looptop to footpoint can be inferred from magnetohydrodynamic simulations of solar flares (Yokoyama and Shibata, 1998; Birn et al., 2009). The mirror ratio for a region near the looptop is therefore expected to be moderate. Using $\tilde{\phi} \sim 0.7$ as determined from simulations, $\tilde{n}_{esp}$ goes down from $\sim$0.24 when no mirror is present to $\sim$0.14 for a moderate mirror ratio of 1.5. Therefore, combining a DL with a

68

moderate mirror substantially enhances the confinement of hot electrons.

5.4 Relevant Observations

Simões & Kontar (2013) presented evidence for electron accumulation at the looptop from a systematic study of solar flares with both looptop and footpoint hard X-ray sources. Magnetic mirroring was considered as a means to trap electrons along the flare loops. To explain the observation, mirror ratios of 2.5 to 5 are needed for isotropic distributions in a more realistic scenario that took into account Compton backscattering at the chromosphere and a neutral target at the footpoint (as opposed to zero backscattering and a fully ionized chromospheric target). Such mirror ratios are higher than estimates of less than 2.1 from investigations of large flare samples of 40-80 flares (Aschwanden et al., 1999; Tomczak and Ciborski, 2007). This suggests that magnetic mirroring alone is not sufficient to trap the electrons at the looptop. As demonstrated in Section 5.3, DL formation, together with a magnetic mirror, can enhance electron trapping. For instance, from Figure 5.3, for a moderate mirror ratio of r=1.5, having a DL with a strength of $\tilde{\phi} \sim 0.7$ traps (1- $\tilde{n}_{esp}$)=(1-0.14)=0.86 of the total electron density while having the mirror alone traps a much lower density of (1-0.4)=0.6. DL formation can, therefore, provide an explanation for electron accumulation at the looptop reported in Simões & Kontar (2013).

Chapter 6

Multiple DLs in large systems

Although DLs have not yet been observed in the solar corona, they are widely seen in various space plasmas, including the solar wind (Mangeney et al., 1999) and the Earth's magnetosphere (Mozer et al., 1985; Ergun et al., 2001, 2009). They are also inferred in the magnetospheres of Jupiter (Hess et al., 2009) and Saturn (Gurnett and Pryor, 2012). In the Earth's plasma sheet, a high number of DLs are detected by the THEMIS (Angelopoulos, 2008) spacecraft during periods of high magnetic activity, implying that DLs may be a frequent occurrence in such situations (Ergun et al., 2009). In the solar atmosphere, magnetic fluctuations are common, especially during flares. Many DLs may similarly occur. In previous chapters, we reported electron confinement by a single DL. The absence of multiple DLs is because of the limited domain size and hence evolutionary time of these systems. In the corona, which is much larger, more DLs could form. The structure of multiple DLs and their interaction with each other can affect electron transport. Understanding this subject is therefore important for future in-situ observations of the corona from missions like NASA's Solar Probe Plus (Guo, 2010). In this work, we investigate possibly new DL dynamics via simulations with larger domains. We find that multiple DLs are generated in larger systems (Li et al., 2013b). The DLs are sustained for the entire course of the simulations, providing an approximately

constant total strength at late time. This is sufficient for significantly confining energetic electrons as demonstrated in Chapter 4.

6.1 Setup for Large-scale Simulations

The initial setup here is the same as in Section 3.1 unless otherwise stated. The initial hot electron temperatures for all simulations are the same: $T_{h0}=1$. We perform four simulations with increasing domain sizes $L_x/L_{x0}=1$, 2, 4 and 8 in the parallel direction. L_{x0} is the length of the smallest run that has a size of $L_{x0} \times L_y=$ 4634.1 × 18.1 λ_{De}^2. The grid size is 0.14×0.14 λ_{De}^2. With increasing domain size, a simulation can be evolved for longer times, which allows us to study long-time behavior of the system. For $T_h=5$ keV, n=10^9 cm^{-3}, which are typical of coronal thermal X-ray sources, $\lambda_{De} \sim 2$ cm. The largest simulation thus has $L_x \sim 1$ km, which is still very short compared with the scale of coronal sources.

6.2 Evolution of DLs in Increasing System Sizes

Figure 6.1 shows the time evolution of the DL strength $e\phi_{DL}$ in simulations of increasing system domain sizes. $e\phi_{DL}$ is measured from the electric field data, which is averaged over one electron plasma period in the two smaller runs and over five periods in the two larger runs. Data is not sampled as frequently in the latter as in the former to improve computational efficiency in the larger systems. Averaging serves to subtract initial electric field fluctuations at the contact of the
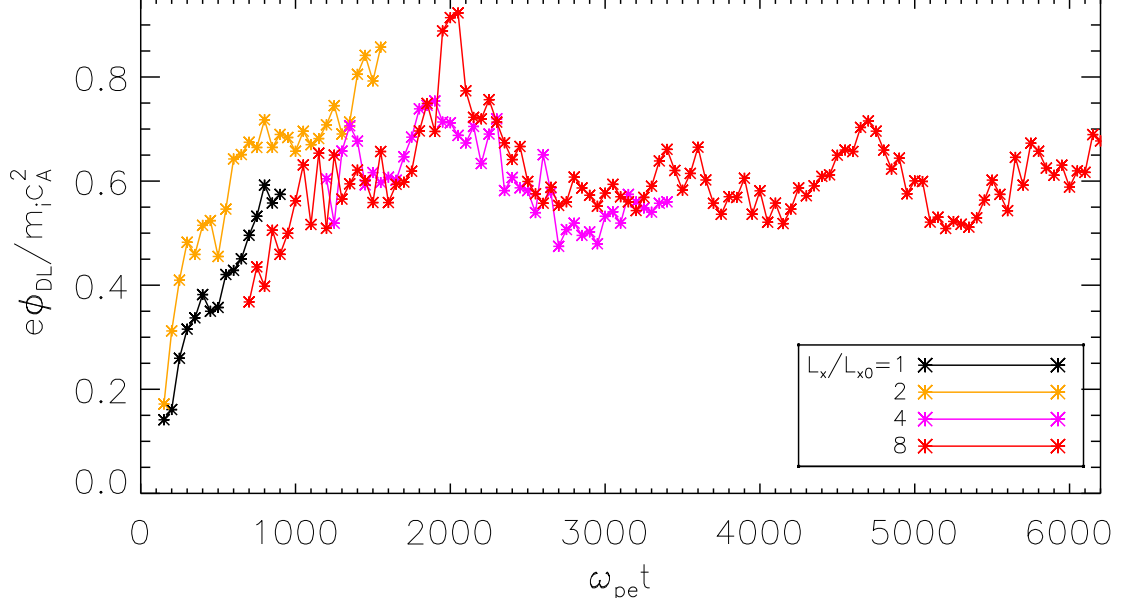
Figure 6.1: Evolution of the DL strength $e\phi_{DL}$ in simulations of increasing system domains.

hot and cold electron regions that fade out after the first $\sim$1200 ω_{pe}^{-1}. Subtraction of the fluctuations is more effective when data are averaged over a shorter time. Therefore, $e\phi_{DL}$ of the smaller runs are smoother while that of the largest run (red) appears to oscillate (about an overall growth trend) before $\omega_{pe}t$=1200, but in general becomes smoother after that time. No averaging is needed after $1200\omega_{pe}^{-1}$ since the averaged and unaveraged data overlap. $e\phi_{DL}$ at early times in the two larger runs are not shown because of these unrealistic oscillations.

The two smaller runs with L_x/L_{x0}=1 and 2 have similar evolutionary trends. The DL(s) in both cases grow, saturate and then grow again. The growth mechanism is explained in Chapter 3 and saturation mechanism in Chapter 4. The late-time trend in the two larger runs deviates from the overally growing tendency observed in the two smaller runs. At late time, $e\phi_{DL}/m_i c_A^2$ settles to an average value of $\sim$ 0.6. We note that the DL strength is sustained throughout the entire course of the

72
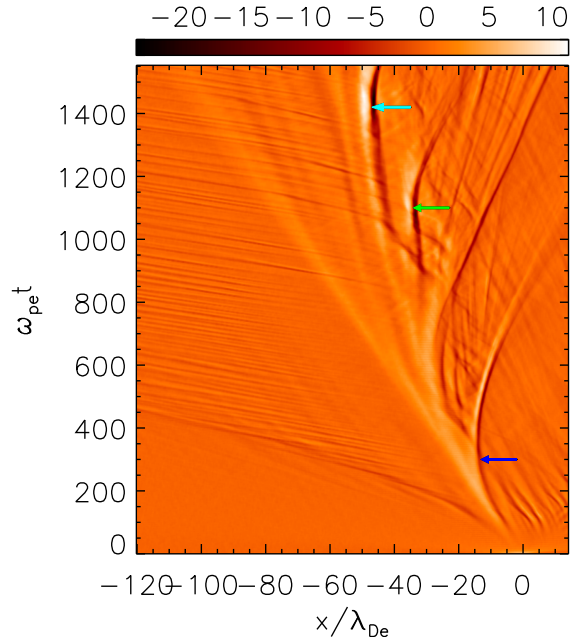
Figure 6.2: Time evolution of the electric field E_x from the $L_x/L_{x0}=2$ run. The top two arrows indicate the position of two DLs and the bottom arrow locates a shock wave.

simulations without showing any signs of decay. In earlier 1D particle simulations in which DLs were driven by a strong applied potential, DLs decayed as many solitons in the form of spiky wave trains propagated toward the high potential side of the DLs (Sato and Okuda, 1981). They were observed to have a lifetime of about 500 ω_{pe}^{-1}, which was equal to the transit time of the solitons across the DL width. In our case, the DLs remain for a much longer time and exhibit no sign of decay.

6.3   Formation of Multiple DLs in Larger Systems

In the smallest run, a single dominant DL is observed. In the second run ($L_x/L_{x0}=2$), a weaker second DL emerges. Figure 6.2 shows the time evolution of the electric field E_x from that run. The bright white feature indicated by a cyan
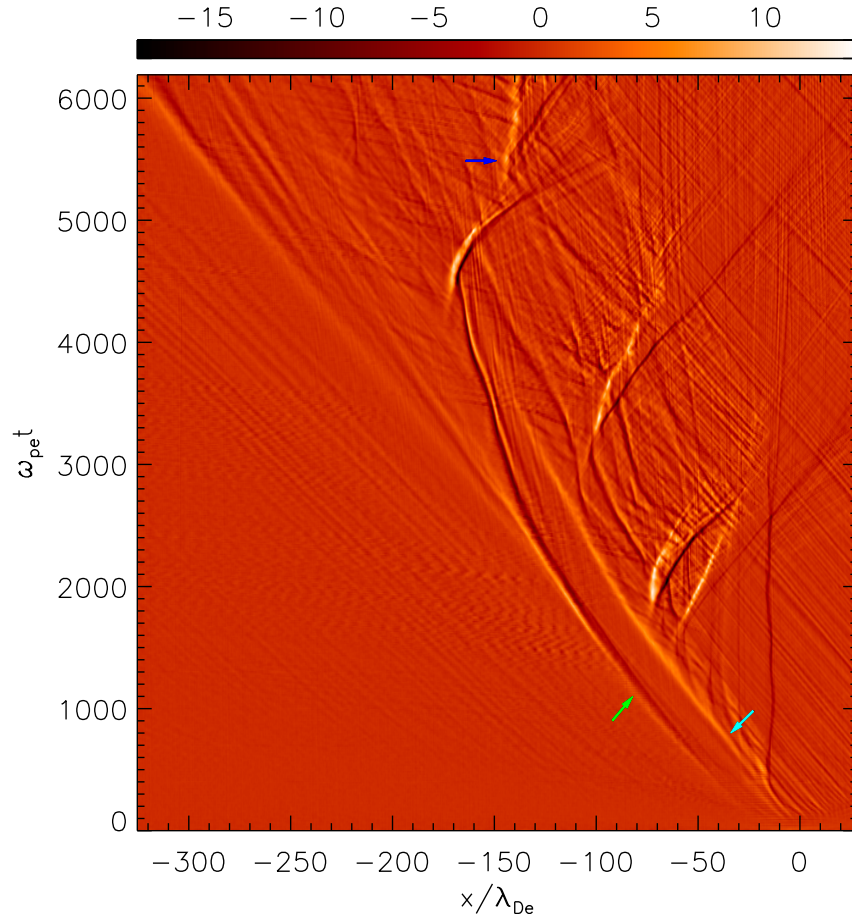
Figure 6.3: Time evolution of the electric field E_x from the largest simulation. Several DLs are indicated by arrows.

arrow (ω_{pe}t~1400) is the dominant DL, and that by a green arrow (ω_{pe}t~1100) is the weaker second DL. Note that a shock wave is generated at ω_{pe}t~300 (blue arrow) and leaves the DL at that time, causing saturation (Chapter 3) of the DL strength from ω_{pe}t=300 to 500 (see the plateauing of the orange curve in Figure 6.1). In the two larger runs (L_x/L_{x0}=4, 8), many DLs are generated. In the following, we focus on data from the largest run to demonstrate the properties and dynamics of multiple DLs. To simplify notation, we drop the units of x and t from here on.

Figure 6.3 is the evolution of E_x from the largest simulation. The first DL (cyan arrow) is the bright feature that emerges at $(x, t) \sim (0, 100)$, and sustains until as late as $t \sim 3500$ at $x \sim$ -140. It strengthens over time and propagates to the left. A shock associated with it forms at $(x, t) \sim (-14, 400)$ and separates from it thereafter. A second DL (green arrow) to the left of the first one becomes apparent at $(x, t) \sim (-45, 400)$. A strong shock with an intense negative electric field is produced by this DL at $t \sim 2600$ and separates from the DL. This will be further discussed later.

6.4   Generation Mechanism for all DLs

The generation mechanism for multiple DLs is the same as that for a single DL. It was identified in Chapter 3 as the Buneman instability that is driven by a cold electron beam as a return current (RC) to the hot electrons that stream through the ambient (cold) plasma. The RC beam drifts with respect to the ions, which excites the instability. In the case of multiple DLs, the first DL can accelerate the original RC beam and the accelerated beam is responsible for the generation of the second DL. Figure 6.4 shows the electron phase space near the contact of the hot and (ambient) cold electrons in early time. In (a), the initial (t=0) electron temperature (green) is overlaid to show the hot and cold regions. To the right of $x \sim 0$ is the cold electron region and to the left is the hot electron region. A RC beam is drawn from the cold electrons into the hot region. On top of initial fluctuations (that is not completely averaged out in the data of this run) in E_x at t=100 (black), the
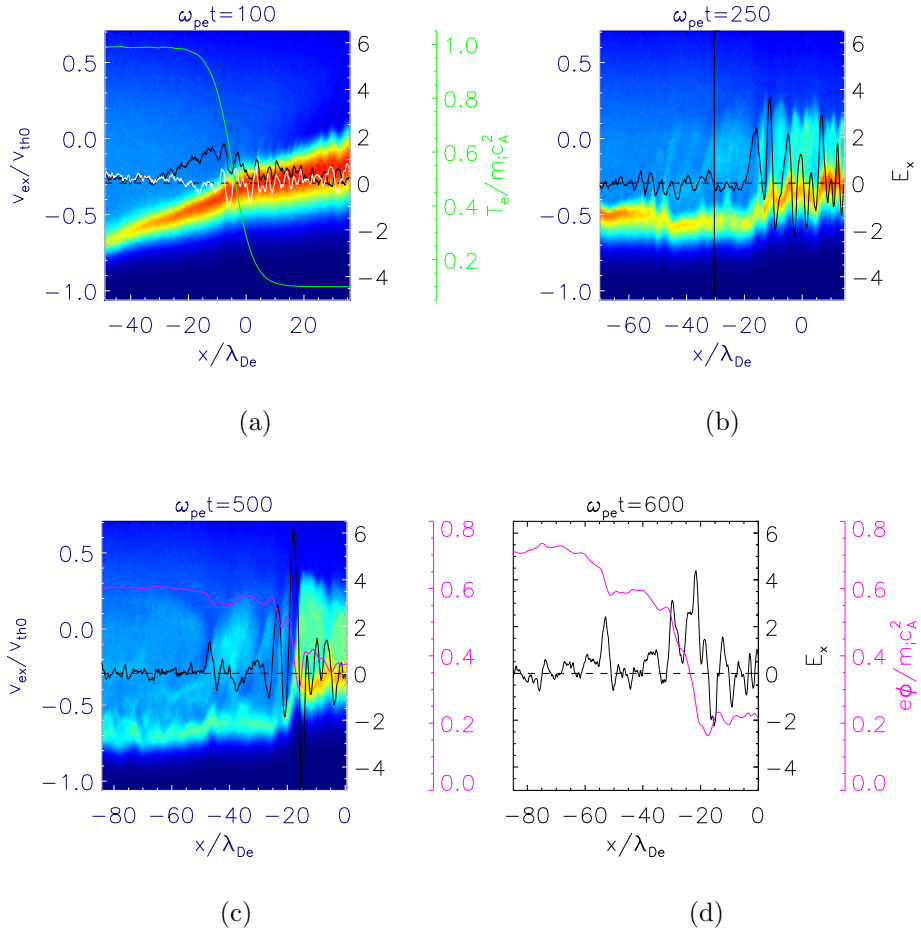
Figure 6.4: Electron phase space, during the emergence of the second DL, at t=100 (a), 250 (b) and 500 (c). Velocities are normalized to the initial hot electron thermal speed. The same color scale is used for all. Overlaid on (a)-(c) and plotted in (d) are E_x (black and white; dashed lines indicate the zero E_x position), the electric potential $e\phi$ (magenta) and the electron temperature T_e at t=0 (green).
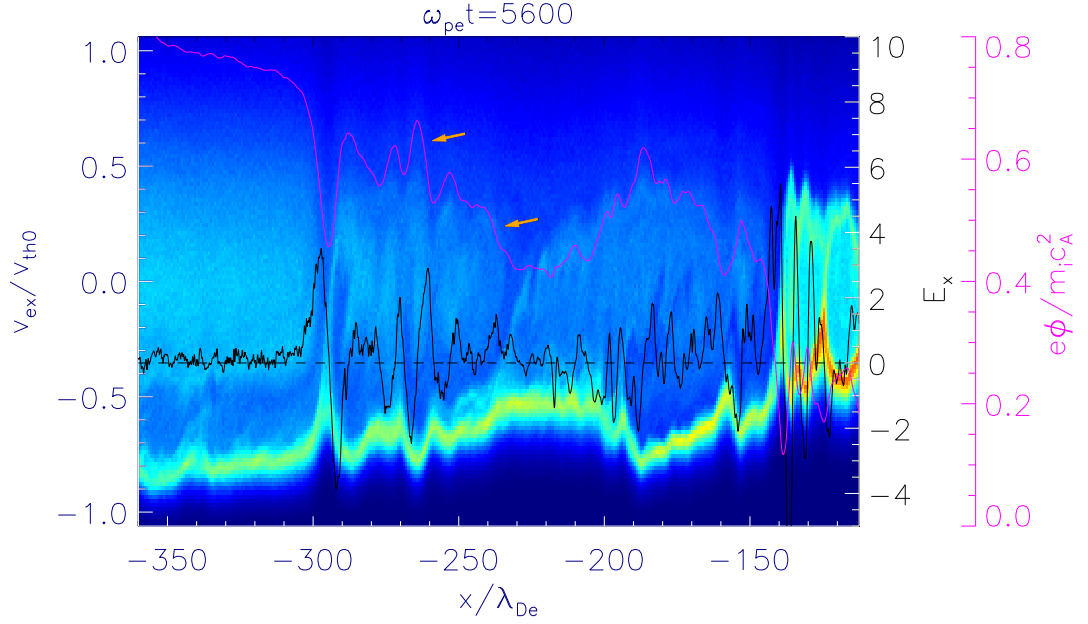
Figure 6.5: Electron phase space at t=5600, a time when many DLs form. Arrows indicate potential drops associated with a couple small DLs between two larger DLs. Same format is used as Figure 6.4.

first DL emerges among the unstable waves near $x \sim$ -10. The second DL is not yet present at this time because shortly after, at t=110 (white), waves present earlier can be seen while no significant feature is observed to the left of $x \sim$ -10. In (b), the (small) second DL appears at the location marked by a vertical black line. The RC beam that is accelerated by the first DL near $x \sim$ -10 is reflected by the second DL – the beam density (cyan) is being dragged from negative to positive velocities near the vertical black line. The reflected beam density behind the second DL (at $x \sim$ -45 in (c)) increases from t=250 (b) to 500 (c). As a result, the DL strengthens noticeably from t=500 to 600 (d) – see the increase in the potential (magenta) drop across the second DL. Therefore, the first DL accelerates the RC beam and seeds the generation of the second DL downstream (to the left) of the first DL.

After a shock forms and departs at $t \sim 2600$, the second DL weakens (Figure 6.3) because the shock stabilizes the instability (Chapter 4) and the DL is no longer driven. However, its potential drop remains nearly stationary. For example, it accounts for one third of the total potential drop at $t=4000$. As the shock diminishes after $t \sim 5000$, the second DL revives. See in Figure 6.3 the gradual brightening at $x \sim$ -270 after $t \sim 5000$. There is also increasing wave activity to the right of the second DL. Around $t \sim 5300$, a third DL, indicated by a blue arrow, develops at $x \sim$ -145 and remains until the end of the simulation. It appears to propagate slowly to the right, opposite to what is usually observed. This is because the ions are accelerated by the second DL, and produce an ambient flow to the right in the region $x >$ -270. Therefore, the third DL is carried by the ambient plasma to the right. Figure 6.5 shows the electron phase space at $t=5600$, some time after the emergence of the third DL. In addition to the second DL (at $x \sim$ -300) and the third DL ($x \sim$ -140) where significant potential jumps occur, a couple of weaker DLs are generated and overall there is substantial wave activity. Orange arrows indicate the associated potential jumps. Note the RC beam is reflected by the negative E_x of the second DL and also by the weaker DLs, for instance, around $x \sim$ -235.

In larger domains that allow the system to evolve for a much longer time, the behavior at late time is much more dynamic than what was seen in smaller domains (Chapter 3, Sato & Okuda 1981). Multiple DLs are generated downstream of the RC beam from a primary DL (the first DL in this case). The growth of these downstream DLs produces an ambient ion flow that pushes the upstream DL further upstream, opening up a space (in between) for more DLs to be generated. A chain

of many DLs can result.
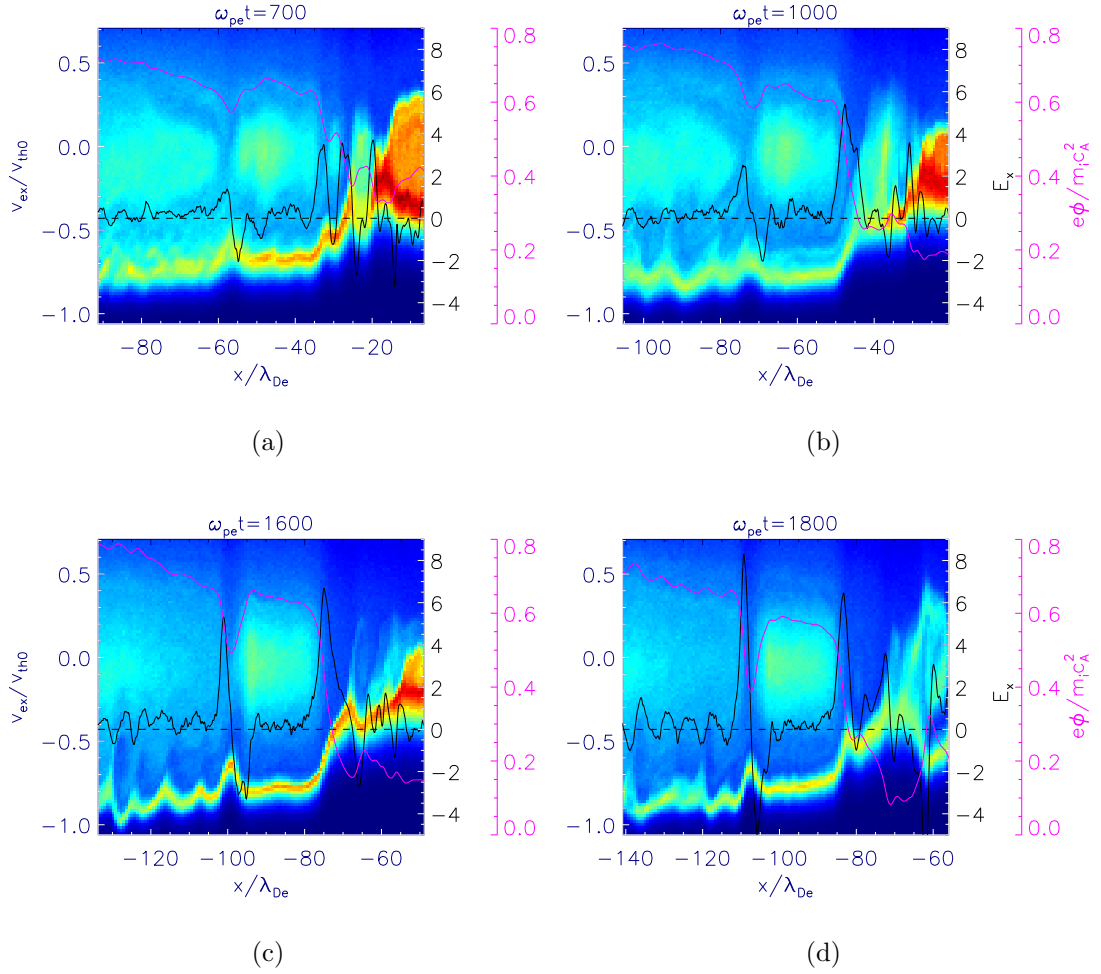
Figure 6.6: Electron phase space at $\omega_{pe}t$=700 (a), 1000 (b), 1600 (c) and 1800 (d), showing electron trapping between two DLs. Same format is used as Figure 6.4.

6.5 Electron Trapping between two DLs

Electron trapping is observed between two DLs. Figure 6.6 shows the time evolution of the electron phase space around two DLs for a period of over 1000 ω_{pe}^{-1}. The electric field of both DLs grows over time. The second DL (on the left in (b),

at $x \sim$ -75) is weaker than the first – see the smaller drop in the potential across it. It develops a large negative E_x (see in (d)), which corresponds to a deep dip in the potential. This dip together with the potential drop at the first DL takes the form of a "cap" (or an inverted potential well). This potential cap can trap electrons. It becomes larger as the dip deepens from (a) to (d). About the same (cyan) population of electrons stay within the cap during this entire period. From (d), these electrons are centered at approximately zero velocity and their velocity range is $\Delta v/v_{th0} \sim \pm 0.3$. Their typical velocity can be taken as their velocity range. The separation between the two DLs is $\Delta x \sim 20$ λ_{De}. The transit time of the electrons between the two DLs is therefore $\tau_{transit} = \Delta x/\Delta v = 20/0.3 \sim 70$ ω_{pe}^{-1}. This is much shorter than the 1000 ω_{pe}^{-1} time scale. Hence, they are trapped between the two DLs. In order to trap these electrons, the potential cap is required to have a depth of $\Delta \phi/T_{h0} \sim \Delta v^2/v_{th0}^2 \sim 0.3^2 \sim 0.1$. In (d), taking the shallower left side, the cap here has a depth of $e\phi_{cap}/T_{h0} \sim 0.2$ (note T_{h0}=1), enough to trap these electrons. The trapped electrons are essentially a peak in phase space since there is an enhancement in phase space density. It has a spatial extent much wider than the typical DL width (of ~ 10 λ_{De}) because two DLs may be widely separated.

6.6   Conclusion on Multiple DLs

In this work, large-scale PIC simulations are performed to explore the possible change in the structure of DLs in a larger, more realistic system. In larger systems, instead of a single DL, multiple DLs are generated. Electron trapping is observed

between two DLs. The DLs sustain for the entire duration of the simulations. The sum of the potential drops of all of the DLs is sufficient for confining a significant fraction of the hot electrons.

Chapter 7

Conclusion and Limitations

7.1   Summary of results

In summary, the transport of flare-heated from the solar corona to the chromosphere is a key issue in understanding the dynamics of flares, but remains poorly understood. Observations of coronal X-ray emissions point to two different pictures of electron transport: free-streaming and confinement of electrons. Confinement is suggested in looptop X-ray emissions, which have a much longer decay time than the transit time of the X-ray producing electrons across the compact source region. Previous solar electron transport models included anomalous conduction due to anomalous resistivity resulting from turbulence. Nevertheless, anomalous conduction has yet to be clearly demonstrated in numerical simulations.

In this thesis, we have presented a mechanism for the suppression of electron transport based on the formation of DLs. We have shown that DL formation substantially suppresses electron transport in PIC simulations. Multiple DLs are generated in large-scale simulations that are not observed in smaller systems. The DLs support a significant jump in the electron temperature between the (hot) electron source and the ambient plasma. We have identified the generation mechanism of the DLs as the Buneman instability between the ions and back-streaming return current electrons. The DLs extract energy and increase their amplitude by the

reflection of the RC electrons.

We have also identified the saturation mechanism of DLs as shock formation. When the potential drop of a DL is large enough to accelerate ions above the local sound speed, a parallel ion acoustic shock results, stabilizing the Buneman instability and subsequently saturating the DL. The shock formation criterion predicts a maximum DL strength that is proportional to the hot electron temperature, in agreement with simulations. We have shown that at the maximum strength, the DL reflects and therefore confines a significant fraction of electrons in the source. The remaining electrons can escape and will likely propagate freely through the ambient plasma.

In large-scale PIC simulations, an increasing number of DLs are formed. The Buneman generation mechanism is the same as in smaller systems. We find, however, that the potential drop across a large DL enhances the RC upstream of the DL and therefore produces an environment that spawns DL formation in this region. The expectation therefore is that real systems such as the corona will produce large numbers of DLs. New dynamics observed in multiple DL systems include the trapping of electrons between DLs and very long lifetimes. These features provide a more realistic picture of DL occurrence in the solar corona that is important for future space missions such as Solar Probe Plus.

This study is potentially important for understanding electron transport in solar flares. We have shown that transport is significantly suppressed as the flare-heated electrons start to propagate away from a coronal acceleration site. A substantial number of electrons are confined by the potential of the DLs while the remainder

can escape. This picture is consistent with both confinement and free-streaming of electrons suggested by observations of coronal X-ray emissions.

7.2   Limitations and Future Work

There are some important limitations of this model. One limitation is that it is effectively 1D since the transverse direction in the 2D simulation domain is only $\approx 20\lambda_{De}$ wide. 2D effects on DLs are not investigated in this study but do not seem to be significant. Extended (planar) weak DLs over 80 λ_{De} in transverse extent were observed in earlier 2D PIC simulations where subthermal electron current was injected at the boundaries of the parallel direction Barnes et al. (1985). Such electron injection may correspond to the return current electrons being drawn in at the contact region of the two electron populations in the present simulations. The planar 2D DLs tend to develop substantial substructure across the magnetic field late in time, but the basic dynamics of the DLs are the same as in 1D. We expect the formation of DLs, and therefore transport suppression of hot electrons, to persist in 2D. However, 2D DLs are unlikely to be planar over $\sim 10^8\lambda_{De}$, the scale of coronal looptops. On the other hand, a variation of the DL over a large transverse distance is not likely to strongly impact the largely 1D dynamics studied here. The injection of a narrow band of hot electrons, however, might produce dynamics different from that studied here. This case remains to be studied.

Another limitation is that the computational size of the PIC simulations, being at most 50000 $\lambda_{De} \sim 1$ km in the corona, is small compared to the actual size of

flaring loops. They, however, reveal important physics down to the kinetic electron scale, the Debye length, where DLs form. We have investigated the possible change of the structure of DLs in larger simulation domains and found additional features but the basic dynamics, particularly the generation mechanism, identified in this model, remains unchanged. Realistic physical systems are expected to produce large numbers of strongly-interacting DLs.

We have modeled the hot electrons as thermal distributions. The coronal HXR sources are usually fit to a combination of a thermal core and a nonthermal tail distribution. Our model has not included the nonthermal tail distribution. However, the DLs are produced by the RC electrons from the ambient plasma. The addition of a nonthermal population is expected to drive a stronger RC and result in stronger DLs. Therefore, the DLs will likely confine a portion of the nonthermal tail. What fraction of the HXR-producing electrons will be confined in this case requires further investigation.

Appendix A

Loss hyperboloid in a DL-mirror configuration

The total energy of an electron in an electric potential $\phi(x)$ and subjected to a magnetic field $B(x)$ is given by

$$W = m_e v_\parallel^2/2 - e\phi(x) + \mu B(x) \tag{A.1}$$

where $\mu = m_e v_\perp^2/2B(x)$ is the magnetic moment. Without other external forces, W is conserved. The potential jump of a DL can be approximated as a step function so that

$$\phi(x) = \begin{cases} \phi_{DL} & x < x_{DL} \\ \\ 0 & x > x_{DL} \end{cases} \tag{A.2}$$

where x_{DL} is the DL position. Before the electron passes through the DL, i.e., $x < x_{DL}$, we have

$$W = \frac{1}{2}m_e v_\parallel^2 - e\phi_{DL} + \mu B_1 \tag{A.3}$$

where B_1 is the value of the magnetic field at some location $x < x_{DL}$. After it passes through the DL and continues to travel until its $v_\parallel$ reaches zero at some point with a magnetic field B_2, so

$$W = \mu B_2. \tag{A.4}$$

Since W is a constant, we equate Equations A.3 and A.4, obtaining

$$
\begin{aligned}
\frac{1}{2}m_e v_\parallel^2 - e\phi_{DL} &= \mu(B_2 - B_1) \\
&= \mu B_1(r-1)\,;\ r \equiv B_2/B_1 \\
&= \frac{1}{2}m_e v_\perp^2(r-1) \\
v_\parallel^2 - v_\perp^2(r-1) &= \frac{2e\phi_{DL}}{m_e}
\end{aligned}
\tag{A.5}
$$

This is a hyperbolic equation in $(v_\parallel, v_\perp)$ space.

Appendix B

Derivation of n_{esp} in a DL-mirror configuration

In this case, the integral is not separable in $v_\parallel$ and $v_\perp$ as it is for n_{esp} in Equation 4.3. In the following, we carry out the full 3D integral over $(v_\parallel, v_\perp, \psi)$, where ψ is the azimuthal angle in the 2D plane spanned by the two perpendicular velocity components. Visualizing the loss hyperboloid in Figure 5.2 in 3D, the other perpendicular velocity axis is directed out of the page. $v_\perp$ of the loss hyperboloid is simply the cross-sectional radius of a cut of the hyperboloid taken at different values of $v_\parallel$ along the $v_\parallel$ axis. This radius is given by $v_{\perp l}^2 = (v_\parallel^2 - b^2)/(r-1)$ (from Equation 5.1), where $b \equiv \sqrt{2\,e\phi_{DL}/m_e}$. We then calculate the escaping electron density:

$$
\begin{aligned}
n_{esp} &= \int_0^{2\pi} d\psi \int_b^\infty dv_\parallel \int_0^{v_{\perp l}} v_\perp dv_\perp \, f_{e0}(v_\parallel, v_\perp) \\
&= 2\pi \int_b^\infty dv_\parallel \int_0^{v_{\perp l}} v_\perp dv_\perp \frac{n_0}{\pi^{3/2} v_{t\parallel} v_{t\perp}^2} \exp\left[-\left(\frac{v_\parallel^2}{v_{t\parallel}^2} + \frac{v_\perp^2}{v_{t\perp}^2}\right)\right] \\
&= \frac{n_0}{\sqrt{\pi} v_{t\parallel}} \int_b^\infty dv_\parallel \, e^{-\frac{v_\parallel^2}{v_{t\parallel}^2}} \left(1 - \exp\left[-\frac{v_\parallel^2 - b^2}{(r-1)v_{t\perp}^2}\right]\right)
\end{aligned}
\tag{B.1}
$$

Defining:

$$a \equiv \frac{1}{v_{t\parallel}^2} \ , \ c \equiv \frac{1}{(r-1)v_{t\perp}^2}$$

$$
\begin{aligned}
n_{esp} &= n_0 \sqrt{\frac{a}{\pi}} \int_b^\infty \mathrm{d}x \left(e^{-ax^2} - e^{cb^2} e^{-(a+c)x^2} \right) \ ; \ x \equiv v_\parallel \\
&= n_0 \sqrt{\frac{a}{\pi}} \left(\int_{b\sqrt{a}}^\infty \frac{\mathrm{d}t}{\sqrt{a}} e^{-t^2} - e^{cb^2} \int_{b\sqrt{a+c}}^\infty \frac{\mathrm{d}s}{\sqrt{a+c}} e^{-s^2} \right) \quad ; \ t \equiv x\sqrt{a}, \ s \equiv x\sqrt{a+c} \\
&= \frac{n_0}{2} \left[\mathrm{erfc}(b\sqrt{a}) - e^{cb^2} \sqrt{\frac{a}{a+c}} \, \mathrm{erfc}(b\sqrt{a+c}) \right]
\end{aligned}
$$

(B.2)

where $\mathrm{erfc}(z) = \frac{2}{\sqrt{\pi}} \int_z^\infty e^{-t^2} \, dt$ is the complementary error function. The total density of hot electrons moving to the right (i.e., the maximum n_{esp} if all hot electrons escape) is:

$$n_{tot} = \int_0^\infty \mathrm{d}^3 v \, f_{e0}(v_\parallel, v_\perp) = \frac{n_0}{2}$$

(B.3)

as expected. Therefore, the fraction of escaping to total density is:

$$\tilde{n}_{esp} = \frac{n_{esp}}{n_{tot}} = \mathrm{erfc}(b\sqrt{a}) - e^{cb^2} \sqrt{\frac{a}{a+c}} \, \mathrm{erfc}(b\sqrt{a+c})$$

(B.4)

Expressing a, b and c in terms of $e\phi_{DL}$, r and temperatures,

$$b\sqrt{a} = \frac{b}{v_{t\parallel}} = \sqrt{\frac{e\phi_{DL}}{T_{\parallel}}} = \tilde{\phi}^{1/2}$$

$$cb^2 = \frac{b^2}{(r-1)v_{t\perp}^2} = \frac{e\phi_{DL}}{T_{\perp}(r-1)}$$

$$= \frac{e\phi_{DL}}{T_{\parallel}}\frac{T_{\parallel}}{T_{\perp}(r-1)} = \frac{\tilde{\phi}}{A(r-1)} \qquad ; \; A \equiv \frac{T_{\perp}}{T_{\parallel}}$$

$$\frac{a}{a+c} = \frac{\frac{1}{v_{t\parallel}^2}}{\frac{1}{v_{t\parallel}^2} + \frac{1}{(r-1)v_{t\perp}^2}} = \frac{1}{1 + \frac{v_{t\parallel}^2}{(r-1)v_{t\perp}^2}} \tag{B.5}$$

$$= \frac{1}{1 + \frac{T_{\parallel}}{T_{\perp}(r-1)}} = \frac{1}{1 + \frac{1}{A(r-1)}}$$

$$b\sqrt{a+c} = \sqrt{b^2\left(\frac{1}{v_{t\parallel}^2} + \frac{1}{(r-1)v_{t\perp}^2}\right)} = \sqrt{\frac{e\phi_{DL}}{T_{\parallel}} + \frac{e\phi_{DL}}{T_{\perp}(r-1)}}$$

$$= \left[\tilde{\phi}\left(1 + \frac{1}{A(r-1)}\right)\right]^{1/2}$$

The final form of $\tilde{n}_{esp}$ is therefore:

$$\tilde{n}_{esp} = \mathrm{erfc}(\tilde{\phi}^{1/2}) - \exp\left[\frac{\tilde{\phi}}{A(r-1)}\right]\frac{1}{\sqrt{1 + \frac{1}{A(r-1)}}}\ \mathrm{erfc}\left(\left[\tilde{\phi}\left(1 + \frac{1}{A(r-1)}\right)\right]^{1/2}\right)$$

$$\tag{B.6}$$

where $A \equiv T_{\perp}/T_{\parallel}$ is a measure of the electron anisotropy.

Bibliography

Akasofu, S.-I., editor (1977). *Physics of magnetospheric substorms*, volume 47.

Angelopoulos, V. (2008). The THEMIS Mission. *Space Science Reviews*, 141:5–34.

Arber, T. D. and Melnikov, V. F. (2009). Thermal fronts in flaring magnetic loops. *ApJ*, 690(1):238.

Aschwanden, M. J., Fletcher, L., Sakao, T., Kosugi, T., and Hudson, H. (1999). Deconvolution of Directly Precipitating and Trap-precipitating Electrons in Solar Flare Hard X-Rays. III.Yohkoh Hard X-Ray Telescope Data Analysis. *ApJ*, 517:977–989.

Aschwanden, M. J., Hudson, H., Kosugi, T., and Schwartz, R. A. (1996a). Electron Time-of-Flight Measurements during the Masuda Flare, 1992 January 13. *ApJ*, 464:985.

Aschwanden, M. J., Kosugi, T., Hudson, H. S., Wills, M. J., and Schwartz, R. A. (1996b). The Scaling Law between Electron Time-of-Flight Distances and Loop Lengths in Solar Flares. *ApJ*, 470:1198.

Aschwanden, M. J. and Schwartz, R. A. (1995). Accuracy, Uncertainties, and Delay Distribution of Electron Time-of-Flight Measurements in Solar Flares. *ApJ*, 455:699.

Aschwanden, M. J., Schwartz, R. A., and Alt, D. M. (1995). Electron Time-of-Flight Differences in Solar Flares. *ApJ*, 447:923.

Barnes, C., Hudson, M. K., and Lotko, W. (1985). Weak double layers in ion-acoustic turbulence. *Physics of Fluids*, 28:1055–1062.

Battaglia, M. and Benz, A. O. (2006). Relations between concurrent hard X-ray sources in solar flares. *A&A*, 456:751–760.

Bernstein, I. B., Greene, J. M., and Kruskal, M. D. (1957). Exact Nonlinear Plasma Oscillations. *Physical Review*, 108:546–550.

Bharuthram, R. and Shukla, P. K. (1986). Multi-dimensional solitons and double layers in a magnetized plasma. *Physica Scripta*, 34:732–735.

Birn, J., Fletcher, L., Hesse, M., and Neukirch, T. (2009). Energy release and transfer in solar flares: Simulations of three-dimensional reconnection. *ApJ*, 695(2):1151.

Biskamp, D. and Chodura, R. (1971). Computer Simulation of Anomalous dc Resistivity. *Physical Review Letters*, 27:1553–1556.

Biskamp, D., von Hagenow, K. U., and Welter, H. (1972). Computer studies of current-driven ion-sound turbulence in three dimensions. *Physics Letters A*, 39:351–352.

Block, L. P. (1978). A double layer review. *Astrophys. Space Sci.*, 55:59–83.

Borovsky, J. E. (1992). Double layers do accelerate particles in the auroral zone. *Physical Review Letters*, 69:1054–1056.

Buneman, O. (1958). Instability, Turbulence, and Conductivity in Current-Carrying Plasma. *Phys. Rev. Lett.*, 1:8–9.

Chanteur, G., Adam, J. C., Pellat, R., and Volokhitin, A. S. (1983). Formation of ion-acoustic double layers. *Physics of Fluids*, 26:1584–1586.

Coakley, P. and Hershkowitz, N. (1979). Laboratory double layers. *Physics of Fluids*, 22:1171–1181.

Dum, C. T., Chodura, R., and Biskamp, D. (1974). Turbulent Heating and Quenching of the Ion Sound Instability. *Physical Review Letters*, 32:1231–1234.

Ergun, R. E., Andersson, L., Tao, J., Angelopoulos, V., Bonnell, J., McFadden, J. P., Larson, D. E., Eriksson, S., Johansson, T., Cully, C. M., Newman, D. N., Goldman, M. V., Roux, A., Lecontel, O., Glassmeier, K.-H., and Baumjohann, W. (2009). Observations of Double Layers in Earth's Plasma Sheet. *Physical Review Letters*, 102(15):155002.

Ergun, R. E., Su, Y.-J., Andersson, L., Carlson, C. W., McFadden, J. P., Mozer, F. S., Newman, D. L., Goldman, M. V., and Strangeway, R. J. (2001). Direct Observation of Localized Parallel Electric Fields in a Space Plasma. *Physical Review Letters*, 87(4):045003.

Goertz, C. K. and Joyce, G. (1975). Numerical Simulation of the Plasma Double Layer. *Astrophysics and Space Science*, 32:165–173.

Guo, Y. (2010). Solar probe plus: Mission design challenges and trades. *Acta Astronautica*, 67(9-10):1063 – 1072.

Gurnett, D. A. and Pryor, W. R. (2012). Auroral Processes Associated With Saturn's Moon Enceladus. *Washington DC American Geophysical Union Geophysical Monograph Series*, 197:305–313.

Hasan, S. S. and Ter Haar, D. (1978). The Alfven-Carlquist double-layer theory of solar flares. *Astrophysics and Space Science*, 56:89–107.

Hasegawa, A. and Sato, T. (1982). Existence of a negative potential solitary-wave structure and formation of a double layer. *Physics of Fluids*, 25:632–635.

Hess, S., Mottez, F., and Zarka, P. (2009). Effect of electric potential structures on Jovian S-burst morphology. *Geophys. Res. Lett.*, 36:14101.

Hollweg, J. V. and Völk, H. J. (1970). New plasma instabilities in the solar wind. *J. Geophys. Res.*, 75(28):5297–5309.

Iizuka, S., Michelsen, P., Rasmussen, J. J., Schrittwieser, R., and Hatakeyama, R. (1985). Double layer dynamics in a collisionless magnetoplasma. *Journal of the Physical Society of Japan*, 54:2516–2529.

Ishiguro, S., Sato, T., Takamaru, H., and Complexity Simulation Group (1997). V-Shaped dc Potential Structure Caused by Current-Driven Electrostatic Ion-Cyclotron Instability. *Physical Review Letters*, 78:4761–4764.

Joyce, G. and Hubbard, R. F. (1978). Numerical simulation of plasma double layers. *Journal of Plasma Physics*, 20:391–404.

Kan, J. R., Lee, L. C., and Akasofu, S.-I. (1979). Two-dimensional potential double layers and discrete auroras. *J. Geophys. Res.*, 84:4305–4315.

Knorr, G. and Goertz, C. K. (1974). Existence and stability of strong potential double layers. *Astrophysics and Space Science*, 31:209–223.

Krall, N. A. and Trivelpiece, A. W. (1973). *Principles of plasma physics*. McGraw-Hill.

Krucker, S., Hudson, H. S., Glesener, L., White, S. M., Masuda, S., Wuelser, J.-P., and Lin, R. P. (2010). Measurements of the Coronal Acceleration Region of a Solar Flare. *ApJ*, 714:1108–1119.

Krucker, S. and Lin, R. P. (2008). Hard X-Ray Emissions from Partially Occulted Solar Flares. *ApJ*, 673:1181–1187.

Krucker, S., White, S. M., and Lin, R. P. (2007). Solar Flare Hard X-Ray Emission from the High Corona. *ApJ Lett.*, 669:L49–L52.

Lacombe, C., Salem, C., Mangeney, A., Hubert, D., Perche, C., Bougeret, J.-L., Kellogg, P. J., and Bosqued, J.-M. (2002). Evidence for the interplanetary electric potential? WIND observations of electrostatic fluctuations. *Annales Geophysicae*, 20:609–618.

Lee, K. W. and Büchner, J. (2011). Collisionless turbulent transport and anisotropic electron heating in coronal flare loops. *A&A*, 535:A61.

Lee, K. W., Büchner, J., and Elkina, N. (2008). Collisionless transport of energetic electrons in the solar corona at current-free double layers. *A&A*, 478:889–895.

Levin, B. N. and Melnikov, V. F. (1993). Quasi-linear model for the plasma mechanism of narrow-band microwave burst generation. *Solar Physics*, 148:325–340.

Li, T. C., Drake, J. F., and Swisdak, M. (2012). Suppression of Energetic Electron Transport in Flares by Double Layers. *ApJ*, 757:20.

Li, T. C., Drake, J. F., and Swisdak, M. (2013a). Coronal Electron Confinement by Double Layers. *ApJ, in press.*

Li, T. C., Drake, J. F., and Swisdak, M. (2013b). *in preparation.*

Liu, W., Petrosian, V., Dennis, B. R., and Jiang, Y. W. (2008). Double Coronal Hard and Soft X-Ray Source Observed by RHESSI: Evidence for Magnetic Reconnection and Particle Acceleration in Solar Flares. *ApJ*, 676:704–716.

Lotko, W. (1983). Reflection dissipation of an ion-acoustic soliton. *Physics of Fluids*, 26:1771–1779.

Lotko, W. (1986). Diffusive acceleration of auroral primaries. *J. Geophys. Res.*, 91:191–203.

Mangeney, A., Salem, C., Lacombe, C., Bougeret, J.-L., Perche, C., Manning, R., Kellogg, P. J., Goetz, K., Monson, S. J., and Bosqued, J.-M. (1999). WIND observations of coherent electrostatic waves in the solar wind. *Annales Geophysicae*, 17:307–320.

Manheimer, W. M. (1977). Energy flux limitation by ion acoustic turbulence in laser fusion schemes. *Physics of Fluids*, 20:265–270.

Manheimer, W. M. and Klein, H. H. (1975). Model for the production and transport of energetic particles in a laser produced plasma. *Physics of Fluids*, 18:1299–1307.

Masuda, S., Kosugi, T., Hara, H., Tsuneta, S., and Ogawara, Y. (1994). A loop-top hard X-ray source in a compact solar flare as evidence for magnetic reconnection. *Nature*, 371:495–497.

Masuda, S., Sato, J., Kosugi, T., and Sakao, T. (2000). Spectral Characteristics of Above-the-Looptop Hard X-Ray Source. *Advances in Space Research*, 26:493–496.

McKean, M. E., Winglee, R. M., and Dulk, G. A. (1990). Modeling solar flare conduction fronts. I - Homogeneous plasmas and ion-acoustic turbulence. *ApJ*, 364:295–321.

Melrose, D. B. (1980). *Plasma astrophysics: Nonthermal processes in diffuse magnetized plasmas*, volume 1.

Miller, J. A., Cargill, P. J., Emslie, A. G., Holman, G. D., Dennis, B. R., LaRosa, T. N., Winglee, R. M., Benka, S. G., and Tsuneta, S. (1997). Critical issues for understanding particle acceleration in impulsive solar flares. *J. Geophys. Res.*, 102:14631–14660.

Mozer, F. S., Boehm, M. H., Cattell, C. A., Temerin, M., and Wygant, J. R. (1985). Large electric fields in the magnetosphere. *Space Science Reviews*, 42:313–335.

Newbury, J. A., Russell, C. T., Phillips, J. L., and Gary, S. P. (1998). Electron temperature in the ambient solar wind: Typical properties and a lower bound at 1 au. *J. Geophys. Res.*, 103(A5):9553–9566.

Nishihara, K., Sakagami, H., Taniuti, T., Hasegawa, A., Michelsen, P., and Rasmussen, J. J. (1982). Symp. on Plasma double layers. *Risø National Laboratory, Roskilde, Denmark*, page 41.

Oreshina, A. and Somov, B. (2011). Heat-transfer mechanisms in solar flares. 1: Classical and anomalous heat conduction. *Moscow University Physics Bulletin*, 66:286–291.

Petrosian, V., Donaghy, T. Q., and McTiernan, J. M. (2002). Loop Top Hard X-Ray Emission in Solar Flares: Images and Statistics. *ApJ*, 569:459–473.

Quest, K. B. (1988). Theory and simulation of collisionless parallel shocks. *Journal of Geophysical Research: Space Physics*, 93(A9):9649–9680.

Quon, B. H. and Wong, A. Y. (1976). Formation of potential double layers in plasmas. *Physical Review Letters*, 37:1393–1396.

Raadu, M. A. (1989). The physics of double layers and their role in astrophysics. *Physics Reports*, 178(2):25 – 97.

Raadu, M. A. and Chanteur, G. (1986). Formation of double layers - Shocklike solutions of an mKdV-equation. *Physica Scripta*, 33:240–245.

Raadu, M. A. and Rasmussen, J. J. (1988). Dynamical aspects of electrostatic double layers. *Astrophys. Space Sci.*, 144:43–71.

Sato, T. and Okuda, H. (1980). Ion-acoustic double layers. *Physical Review Letters*, 44:740–743.

Sato, T. and Okuda, H. (1981). Numerical simulations on ion acoustic double layers. *J. Geophys. Res.*, 86:3357–3368.

Schamel, H. (1983). Weak Double Layers: Existence, Stability, Evidence. *Zeitschrift Naturforschung Teil A*, 38:1170.

Shawhan, S. D. (1976). Io sheath-accelerated electrons and ions. *J. Geophys. Res.*, 81:3373–3379.

Simões, P. J. A. and Kontar, E. P. (2013). Implications for electron acceleration and transport from non-thermal electron rates at looptop and footpoint sources in solar flares. *A&A*, 551:A135.

Singh, N. (1982). Double layer formation. *Plasma Physics*, 24:639–660.

Singh, N. and Schunk, R. W. (1982). Dynamical features of moving double layers. *J. Geophys. Res.*, 87:3561–3580.

Singh, N., Thiemann, H., and Schunk, R. W. (1985). Dynamical features and electric field strengths of double layers driven by currents. *J. Geophys. Res.*, 90:5173–5186.

Singh, N., Thiemann, H., and Schunk, R. W. (1987). Electric fields and double layers in plasmas. *Laser and Particle Beams*, 5:233–255.

Smith, D. F. and Lilliequist, C. G. (1979). Confinement of hot, hard X-ray producing electrons in solar flares. *ApJ*, 232:582–589.

Spitzer, L. (1962). *Physics of Fully Ionized Gases.*

Temerin, M., Cerny, K., Lotko, W., and Mozer, F. S. (1982). Observations of double layers and solitary waves in the auroral plasma. *Physical Review Letters*, 48:1175–1179.

Tomczak, M. and Ciborski, T. (2007). Footpoint versus loop-top hard X-ray emission sources in solar flares. *A&A*, 461:315–323.

Torven, S. (1981). Modified Korteweg-de Vries equation for propagating double layers in plasmas. *Physical Review Letters*, 47:1053–1056.

Torvén, S. and Babić, M. (1975). Current chopping space charge layers in a low pressure arc plasma. In Hölscher, J. G. A. and Schram, D. C., editors, *Phenomena in Ionized Gases, Twelfth International Conference*, page 124.

Tsuneta, S., Masuda, S., Kosugi, T., and Sato, J. (1997). Hot and Superhot Plasmas above an Impulsive Flare Loop. *ApJ*, 478:787.

Tsytovich, V. N. (1971). The spectra and correlation functions for ion sound turbulence. *Plasma Physics*, 13:741–756.

Williams, A. C., Weisskopf, M. C., Elsner, R. F., Darbro, W., and Sutherland, P. G. (1986). Accretion onto neutron stars with the presence of a double layer. *ApJ*, 305:759–766.

Yokoyama, T. and Shibata, K. (1998). A Two-dimensional Magnetohydrodynamic Simulation of Chromospheric Evaporation in a Solar Flare Based on a Magnetic Reconnection Model. *ApJ*, 494:L113.

Zeiler, A., Biskamp, D., Drake, J. F., Rogers, B. N., Shay, M. A., and Scholer, M. (2002). Three-dimensional particle simulations of collisionless magnetic reconnection. *J. Geophys. Res.*, 107:1230.